Advanced modeling of higher-order kinematic hardening in strain gradient crystal plasticity based on discrete dislocation dynamics

Yaovi Armand AMOUZOU-ADOUN[a], Mohamed JEBAHI[a], Samuel FOREST[b], Marc FIVEL[c]

[a]*Arts et Metiers Institute of Technology, CNRS, Université de Lorraine, LEM3, F-57000 Metz, France*
[b]*Mines Paris, PSL University, Centre des matériaux (CMAT), CNRS UMR 7633, BP 87, 91003 Evry, France*
[c]*Univ. Grenoble Alpes, CNRS, Grenoble INP, SIMaP, F-38000 Grenoble, France*

Abstract

An extensive study of size effects on the small-scale behavior of crystalline materials is carried out through discrete dislocation dynamics (DDD) simulations, intended to enrich strain gradient crystal plasticity (SGCP) theories. These simulations include cyclic shearing and tension-compression tests on two-dimensional (2D) constrained crystalline plates, with single- and double-slip systems. The results show significant material strengthening and pronounced kinematic hardening effects. DDD modeling allows for a detailed examination of the physical origin of the strengthening. The stress-strain responses show a two-stage behavior, starting with a micro-plasticity regime with a steep hardening slope leading to strengthening, and followed by a well-established hardening stage. The scaling exponent between the apparent (higher-order) yield stress and the geometrical size h varies depending on the test type. Scaling relationships of $h^{-0.2}$ and $h^{-0.3}$ are obtained for respectively constrained shearing and constrained tension-compression, aligning with some experimental observations. Notably, the DDD simulations reveal the occurrence of the uncommon type III (KIII) kinematic hardening of Asaro in both single- and double-slip cases, emphasizing the relevance of this hardening type in the realm of small-scale plasticity. Inspired by insights from DDD, two advanced SGCP models incorporating alternative descriptions of higher-order kinematic hardening mechanisms are proposed. The first model uses a Prager-type higher-order kinematic hardening formulation, and the second employs a Chaboche-type (multi-kinematic) formulation. Comparison of these models with DDD simulation results underscores their ability to effectively capture the observed strengthening and hardening effects. The multi-kinematic model, through the use of quadratic and non-quadratic higher-order potentials, shows a notably better qualitative congruence with DDD findings. This represents a significant step towards accurate modeling of small-scale material behaviors. However, it is noted that the proposed models still have limitations, especially in matching the DDD scaling exponents, with both models producing h^{-1} scaling relationships (*i.e.,* Orowan relationship for precipitate size effects). This indicates the need for further improvements in gradient-enhanced theories in order to guarantee their suitability for practical engineering applications.

Keywords: Discrete dislocation dynamics; Strain gradient crystal plasticity; Cyclic loading; Higher-order kinematic hardening; Strengthening; Size effects

1. Introduction

The need to address environmental constraints and the rapid evolution of Micro Electro-Mechanical Systems (MEMS) have led to a demand for thinner and smaller structures. It is fundamental to have a deep

Email addresses: yaovi.amouzou-adoun@ensam.eu (Yaovi Armand AMOUZOU-ADOUN), mohamed.jebahi@ensam.eu (Mohamed JEBAHI), samuel.forest@minesparis.psl.eu (Samuel FOREST), marc.fivel@simap.grenoble-inp.fr (Marc FIVEL)

understanding of the material behavior at small-scales. Several experimental works have shown a size-dependent response of metallic materials at small-scales (E. O. Hall, 1951; Thompson, 1977; Fleck et al., 1994; Stölken and Evans, 1998; Xiang and Vlassak, 2006; Xie et al., 2023; Zhang et al., 2023). A "smaller is stronger" effect over scales ranging from a fraction of a micron to a few tens of microns is observed, manifesting an increase in hardening and/or strengthening (increase of the yield stress) as the geometrical size h decreases. Typically, the yield stress is found to evolve as h^{-r}, with the scaling exponent $r \geq 0$ subject of intense debates (Dunstan and Bushby, 2014; Cordero et al., 2016) as it will be discussed in the present paper. It is firmly believed that these effects are related to the the so-called concept of geometrically necessary dislocations (GNDs; Ashby, 1970). During deformation at small-scales, non-uniform plastic deformation arises and GNDs are essential to accommodate the crystal lattice curvature. Knowing the complications involved in small-scale experiments, numerical approaches are essential to handle complex applications. Although having great capabilities, conventional plasticity theories fall short in modeling size effects due to the absence of internal length scales.

Alongside with molecular dynamics (Zhu et al., 2011; Xing et al., 2021) and discrete dislocation dynamics (DDD) (Shu et al., 2001; Motz et al., 2008; Kiener et al., 2010; Motz and Dunstan, 2012; El-Awady et al., 2013; Amouzou-Adoun et al., 2023; Jian et al., 2024), strain gradient plasticity (SGP) presents very promising capabilities to capture such effects. Since the seminal papers of Aifantis (Aifantis, 1984, 1987), various SGP theories have been intensively developed for both single- and poly-crystal structures, see, *e.g.,* the non-exhaustive list (Fleck et al., 1994; Gurtin, 2002; Gudmundson, 2004; Gurtin et al., 2007; Bardella, 2010; Cordero et al., 2010; Fleck et al., 2014; Bardella and Panteghini, 2015; Dahlberg and Boåsen, 2019; Dahlberg and Ortiz, 2019; El-Naaman et al., 2019; Panteghini et al., 2019; Cai et al., 2021; Jebahi and Forest, 2021; Kuroda et al., 2021; Croné et al., 2022; Jebahi and Forest, 2023; Mukherjee and Banerjee, 2023). The present work focuses here on higher-order models, as Niordson and Hutchinson (2003) have demonstrated that lower-order models (Aifantis, 1984, 1987; Acharya and Bassani, 2000; Busso et al., 2000) can lead to likely unacceptable behaviors with spurious mesh dependence for some problems. Indeed, lower-order models only include strain gradient terms in the classical yield condition while keeping conventional stresses, equilibrium equations and boundary conditions of conventional plasticity. On the contrary, higher-order theories include additional plastic variable(s) as degree(s) of freedom along with the classical displacement field, leading to new higher-order stresses (gradient-conjugate stresses), supplementary balance equations and boundary conditions. These additional degrees of freedom can be scalar-based, like the cumulative plastic strain p (Aifantis, 1987; Gudmundson, 2004), the plastic slip γ (Gurtin, 2002; Gurtin et al., 2007; Jebahi and Forest, 2023), the cumulative plastic slip γ_{eq} (Bayerschen and Böhlke, 2016; Scherer et al., 2020), the equivalent plastic strain ε_{eq} (Jebahi and Forest, 2021) or tensor-based, like the full plastic strain $\boldsymbol{\varepsilon}_p$ (Gudmundson, 2004; Fleck et al., 2014) or the plastic distortion $\mathbf{H}_p$ (Forest, 2008; Cordero et al., 2010). The interest in this paper is on higher-order γ-based strain gradient crystal plasticity (SGCP) models which are able to model orientation effect (anisotropic behavior). Recent experiments on single-crystals (Zhang et al., 2023) have highlighted the need to improve this type of models.

To date, higher-order theories have demonstrated the most promising capabilities in modeling size effects. The emerging issue of expressing the higher-order stresses is the focus of ongoing debates. Two approaches can possibly be distinguished: "parallel models" and "series models". The "parallel models" are based on the decomposition of the higher-order stresses into energetic (recoverable) and dissipative (unrecoverable) parts. Based on the modeling assumptions for the dissipative parts of the higher-order stresses, Hutchinson (2012) distinguished two classes of SGP theories: (i) incremental theories, in which the higher-order dissipative stresses are expressed incrementally as a function of the increments of plastic variables and their gradients, and (ii) non-incremental theories (also called Gurtin-type), in which the higher-order dissipative stresses are themselves related to the increments of the plastic variables and their gradients. The model proposed by Fleck and Hutchinson (2001) belongs to the first class of incremental theories. Although providing interesting features in size effect modeling, incremental models have been

proven to violate the second law of thermodynamic (non-negative dissipation) for some problems (Gudmundson, 2004; Gurtin and Anand, 2009). Given that no experimental evidence proves the assumption of dropping the higher-order dissipation, it is necessary to find different ways to express it (Voyiadjis and Deliktas, 2009). Non-incremental (Gurtin-type) approaches have been formulated to ensure the non-negative dissipation conditions (Gurtin, 2004; Gurtin et al., 2007), making them the most commonly used in the literature (Gurtin and Anand, 2009; Forest and Bertram, 2011; Panteghini and Bardella, 2018; El-Naaman et al., 2019; Martínez-Pañeda et al., 2019; Forest, 2020; Jebahi and Forest, 2021, 2023). Nevertheless, as highlighted by several works (Fleck et al., 2014, 2015; Voyiadjis and Song, 2016; Panteghini et al., 2019; Jebahi et al., 2020), these non-incremental theories always exhibit uncommon effects known as "elastic-gaps" under certain non-proportional loading conditions. These gaps appear to be a macroscopic manifestation of an interruption in the plastic regime following an infinitesimal change in the boundary conditions until a new yield point is reached. In a previous work by the authors (Amouzou-Adoun et al., 2023), it has been demonstrated that advanced DDD simulations did not reveal any traces of "elastic-gaps". This finding supports the non-physical nature of these gaps and raises questions regarding the ability of classical non-incremental SGP approaches to model higher-order dissipation. For a further detailed discussion of these "parallel models" and their potential comparison with experimentally observed size effects, the reader can refer to Voyiadjis and Song (2019). "Series models" represent the next generation of gradient-enhanced models aiming to avoid such gaps while taking into account thermodynamically-consistent higher-order dissipation. These models are based on the higher-order kinematic decomposition of the gradients of the additional plastic variables into energetic and dissipative parts. Within generalized continua, kinematic decomposition techniques have inspired several works on Cosserat media (de Borst, 1993; Forest et al., 1997; Forest and Sievert, 2003), micromorphic approaches (Forest and Sievert, 2003; Forest, 2009; Regueiro, 2010) and strain gradient continua (Fleck and Hutchinson, 1997; Gologanu et al., 1997). Using this type of approach in the context of phenomenological (or isotropic) SGP, the recent work of Panteghini et al. (2019) has been the first to remove "elastic-gaps" while including thermodynamically-consistent higher-order dissipation with multiple simple quadratic defect energy functions. Jebahi and Forest (2023) applied a similar decomposition technique to an γ-based SGCP, showcasing the elimination of these gaps. The proposed model can only reproduce higher-order isotropic hardening. Meanwhile, experimental (Hidayetoglu et al., 1985; Xiang and Vlassak, 2006; Kiener et al., 2010) and numerical (Jiang et al., 2019; Amouzou-Adoun et al., 2023; Ugi et al., 2024) works show a predominant kinematic hardening with respect to the isotropic hardening at small-scales. Given the effect of GNDs, it is necessary to have a meticulous consideration of kinematic hardening. In the present work, higher-order kinematic hardening techniques will be discussed within SGCP "series models" framework. The aim here is to transfer the great capabilities of Prager- and Chaboche-like hardening models commonly used in conventional plasticity (Besson et al., 2010) to higher-order context.

Given the challenges posed by real small-scale experiments, dialogue between SGCP and DDD is a suitable way to enrich SG(C)P theories (Shu et al., 2001; Bittencourt et al., 2003; Yefimov et al., 2004; Bardella et al., 2013; Bayerschen et al., 2015; Chang et al., 2016; Amouzou-Adoun et al., 2023). In fact, DDD is a powerful physics-based numerical tool that accurately characterizes small-scale plasticity by accounting for dislocation activity with minimal modeling assumptions. DDD will then serve as a reference to the present developments in constitutive continuum crystal plasticity modeling. Through the Burgers vector associated with the dislocation lines, serving as intrinsic internal length scale, DDD can naturally reproduce challenging experimentally observed size effects (Motz et al., 2008; Kiener et al., 2010; Motz and Dunstan, 2012; El-Awady et al., 2013; Gravell and Ryu, 2020; Amouzou-Adoun et al., 2023). Under uniaxial tensile loading conditions, investigations on the dependence of the flow stress with the geometrical size have been undertaken (Zhou et al., 2010; Ryu et al., 2020). Micro-bending of thin foils (Motz et al., 2008; Kiener et al., 2010; Motz and Dunstan, 2012), micro-torsion of thin wires (Ryu et al., 2016) or nano-indentation (Fivel et al., 1998; Robertson and Fivel, 1999) simulations with DDD have shown agreement with experimental observations. Bittencourt et al. (2003) presented one of the first comparative studies between the Gurtin-type

SGCP model (Gurtin, 2002) and DDD on two-dimensional (2D) single-crystal boundary value problems. Using quadratic defect energy and isotropic-like hardening (first-order), the authors show that heterogeneous distribution of the plastic strain and the macroscopic stress-strain curves from DDD are reproduced by the non-local SGCP theory. Bardella et al. (2013) have also utilized a Gurtin-type theory in comparison to DDD to investigate the shearing problem under monotonic loading. The paper focused on describing latent isotropic-type hardening, without highlighting the strengthening mechanism. Chang et al. (2016) have followed similar path by comparing DDD results with the micromorphic formulation of the so-called "$\mathrm{curl}\,\mathbf{H}_p$" SGP model. Fully cyclic loading have not been the focus of these works. Therefore, an in-depth investigation of size effects under cyclic loading within DDD and SGCP frameworks is necessary as suggested in the literature (Bardella et al., 2013; El-Naaman et al., 2019). In this work, DDD simulations on cyclic shearing and tension-compression will be conducted on a single-crystal. An accent will be put on the uncommon type III (KIII) kinematic hardening of Asaro (Asaro, 1975; Hidayetoglu et al., 1985). Another important issue tackled in this paper is the understanding of the mechanism of strengthening (increasing yield strength with decreasing size). The scaling exponent will then be discussed. Insights gleaned from DDD simulations will be utilized to improve the SGCP "series model" proposed by Jebahi and Forest (2023). The capabilities of this model will be extended by incorporating Prager- and Chaboche-like higher-order kinematic hardening. The physical meaning of the introduced parameters will be demonstrated based on the observed phenomena in DDD simulations.

After this introduction, the present paper is structured as follows. Section 2 presents a thorough analysis of size effects in cyclic shearing and tension-compression boundary problems using DDD. These findings serve as a reference for further development in SGCP. Section 3 provides the theoretical aspects of the two proposed higher-order kinematic hardening models, namely Prager-type and Chaboche-type (multi-kinematic) models. Section 4 presents an analytical resolution of purely energetic problem with generalized non-quadratic defect energy, in order to validate the implementation and to facilitate the fitting with DDD. SGCP simulations and dialogue with DDD are highlighted in Section 5. Finally, Section 6 presents some concluding remarks and recommendations.

2. Investigation of size effects with DDD

In this section, an extensive DDD investigation of size effects in single-crystals is realized in order to serve as a reference prior to the development of continuum approaches that will be introduced later on. Cyclic shearing and tension-compression tests under quasi-static conditions are conducted to have a better understanding of the strengthening phenomenon and the non-linear kinematic hardening dependence with the geometrical size. Single- and double-slip configurations are employed to emphasize the observations. The material parameters used are listed in Tab. 1.

2.1. General DDD approach and problem description

The DDD simulations are performed with the 3D code TRIDIS (Fivel et al., 1996; Verdier et al., 1998; Amouzou-Adoun et al., 2023) which is based on the explicit representation of dislocation lines in 3D, discretized into successions of pure screw and edge segments embedded in an elastic medium. Under the effect of the Peach-Koehler force (Peach and Koehler, 1950), each dislocation moves at a velocity v calculated by a linear mobility law given by:

$$v = \frac{\tau_{\text{eff}}}{B} b \tag{1}$$

with b the magnitude of the Burgers vector $\mathbf{b}$, B the phonon drag coefficient and τ_{eff} the effective resolved shear stress. The latter variable is defined by:

$$\begin{cases} \tau_{\text{eff}} = \left(|\tau^*| - \tau_{\text{Peierls}} \right)^+ \text{sign}(\tau^*) \\ \tau^* = \left[\left(\dfrac{1}{b} [\hat{\boldsymbol{\sigma}} + \tilde{\boldsymbol{\sigma}}] \mathbf{b} \right) \times \mathbf{l} \right] \cdot \mathbf{g} + \tau_{\text{lt}} \end{cases} \tag{2}$$

where $\left(\bullet \right)^+$ represents the positive part of the item $\bullet$, $\mathbf{l}$ denotes the line vector of the considered dislocation segment, $\mathbf{g}$ is the glide direction vector, τ_{lt} is the line tension which accounts for the local curvature of a dislocation, $\hat{\boldsymbol{\sigma}}$ is the applied stress, $\tilde{\boldsymbol{\sigma}}$ is the internal stress generated by the dislocation network in an infinite medium as formulated by Cai et al. (2006) and τ_{Peierls} stands for the lattice friction which acts as a source of resistance to dislocation motion. The DDD code used in this work is a 3D version (*i.e.,* grains are represented in 3D and dislocation lines evolve in the 3D space, *e.g.,* as presented in Fig. 1a). However, it can be employed for comparison with continuum 2D problems while retaining the advantages of a 3D formulation (Chang et al., 2016). It is necessary to make certain adaptations, as will be described subsequently, while keeping the 3D dislocation line evolution (in particular the formation of loops).

For the sake of comparison with SGCP 2D problems, an idealized 3D DDD setup is enforced (see Fig. 1a). First, the considered domains have periodic boundary conditions along the direction $\mathbf{e}_1 = [100]$ and finite sizes h along the direction $\mathbf{e}_2 = [010]$. In the direction $\mathbf{e}_3 = [100]$, the domains are sufficiently thick and possess periodic boundary conditions. Second, the edge dislocation lines are chosen to be parallel to $\mathbf{e}_3 = [001]$. Third, the screw dislocations lines are contained in the plane $(\mathbf{e}_1, \mathbf{e}_2)$. This means that, in single-slip case, the Burgers vector is defined as $\mathbf{b}_1 = b\,[\cos\theta_1\,\mathbf{e}_1 + \sin\theta_1\,\mathbf{e}_2]$, with θ_1 an angle. In the case of double-slip case, two Burgers vectors are defined as $\mathbf{b}_1 = b\,[\cos\theta_1\,\mathbf{e}_1 + \sin\theta_1\,\mathbf{e}_2]$; $\mathbf{b}_2 = b\,[\cos\theta_2\,\mathbf{e}_1 + \sin\theta_2\,\mathbf{e}_2]$, with $\theta_1 = -\theta_2$ (two symmetrical systems oriented at θ_1 and θ_2 angles). For simplicity, θ_1 is taken to be 60° in the entire work. It is important to note that although the studied 3D box leads to 3D dislocation configurations and structures, this approach provides a reference for comparison with 2D plane strain continuum theories. Fig. 1b and 1c illustrate the considered geometrical 2D shearing and tension problems. Moreover, at the beginning, edge Frank-Read sources (FRs) with varying finite initial lengths are randomly distributed on the slip plane(s) to create the initial dislocation network. The effect of the initial dislocation density ρ_0^{DDD} on the flow stress have been discussed previously in the literature (El-Awady, 2015; Fan et al., 2021; Amouzou-Adoun et al., 2023). Several works (Byer and Ramesh, 2013; El-Awady et al., 2013; Gravell and Ryu, 2020; Cruzado et al., 2024) show that the ρ_0^{DDD} can affect the scaling law. In the context of this work, the initial dislocation density is chosen to be $\rho_0^{DDD} = 3 \times 10^{12}\ \text{m}^{-2}$ for all the simulations. For a given initial configuration (*e.g.,* a fixed geometrical size), three different samples with randomly generated FRs are used to alleviate statistical effects. The macroscopic response associated with each sample will be plotted for all the simulations. It is important to note that DDD results typically exhibit oscillations. Therefore, when conducting scaling relationship analysis, any stress extracted at a specific value of plastic strain is considered to be the moving average stress around this value.

Passivation conditions are enforced at the top and bottom surfaces (in the direction $\mathbf{e}_2$) located respectively at $h/2$ and $-h/2$ in order to create GND effects (*i.e.,* dislocation are blocked at these surfaces). As the applied loading increases, dislocations move and interact with each other within the studied domain. When they encounter the passivated surfaces, they become immobilized. Immobilization of these dislocations against the passivated surfaces leads to the formation of dislocation pile-ups at these boundaries, forming GND walls which significantly contribute to size effects. The cyclic shearing and tension-compression are performed such that the plastic strain (*i.e.,* ε_{12}^p in shearing and ε_{11}^p in tension-compression) increases from 0% to 0.1% (monotonic loading), then decreases from 0.1% to -0.1% (reversed loading) and finally increases again from -0.1% to 0%. This gives the full cyclic path $0\% \rightarrow 0.1\% \rightarrow -0.1\% \rightarrow 0\%$. Fig. 2 displays the evolution of the dislocation structure during the shearing loading process. It can be observed

Tab. 1. DDD parameters based on those of Nickel as documented in the literature (El-Awady et al., 2013; Hussein et al., 2015; Gravell and Ryu, 2020).

Material parameter name	Symbol	Value	Unit
Shear modulus	μ	75200	MPa
Poisson ratio	ν	0.376	$--$
Burgers vector magnitude	b	2.489	Å
Friction stress	τ_{Peierls}	37.6	MPa
Drag coefficient	B	1.1×10^{-5}	$\text{Pa} \cdot \text{s}$

that dislocations accumulate at the passivated surfaces. In addition, a significant number of infinite edge dislocations are observed as a consequence of the periodic boundary conditions and the passivation. Finite length curved and infinite length straight dislocations then coexist during loading. Although, the shearing and tensile boundary problems described are well documented in the literature (Bittencourt et al., 2003; Gurtin et al., 2007; Bardella et al., 2013; Mayeur and McDowell, 2013; Fleck et al., 2014; Chang et al., 2016; Kuroda and Needleman, 2023), new interesting insights into the understanding of plasticity at small-scale will be provided, with a particular focus on strengthening and size effects under cyclic loading.

2.2. Size effects results

Analyzing the double-slip case under cyclic shearing, size effects are visible as presented in Fig. 3. Specifically, Fig. 3a shows the macroscopic response for several different geometrical sizes h in terms of stress σ_{12} as a function of the plastic strain ε^p_{12}. Fig. 3b shows the equivalent response in terms of stress σ_{12} as a function of the total strain ε_{12}. Fig. 3c presents the particular observed features on the plastic activity. This effort is being made to emphasize the outcomes. Focusing on the monotonic loading phase of shearing (*i.e.,* $\varepsilon^p_{12} : 0 \rightarrow 0.1\%$), the increase of the yield stress and the hardening slope with the decrease of the geometrical size h is clearly observed. In Figs. 3a and 3c, two distinct parts of the plastic activity can be magnified. A first micro-plasticity regime, which is evidenced for low plastic strain level (generally ε^p_{12} is less than 0.02%) and is also characterized by a high hardening slope H_1 until a shifting stress, can be distinguished. This micro-plasticity regime is a consequence of dislocation curvature through the line tension effects, their interaction with each other and with the passivated surfaces at the initial stage of plasticity. The shifting stress, referred to hereafter as the apparent higher-order yield stress σ^{HO}_{12}, is observed to be dependent on the size h. The hardening slope H_1 also varies with h. This mechanism is considered to be responsible for the strengthening phenomenon as experimentally observed in the literature (Xiang and Vlassak, 2006; Hua et al., 2021; Xie et al., 2023, 2024). It differs from the common interpretation within SGP which states that strengthening is a delay of the onset of plastic flow until the apparent higher-order yield stress is reached (*i.e.,* the behavior prior to the apparent higher-order yield stress is considered purely elastic). Such a delay is commonly called "elastic-gap" at initial yield (Fleck et al., 2014). Thus, the apparent higher-order yield stress is plotted against the geometrical size h in a log-log space in Fig. 4a. It is shown that σ^{HO}_{12} evolves as $h^{-0.2}$ scaling relationship:

$$\sigma^{HO}_{12} \propto h^{-0.2} \tag{3}$$

similarly to some experimental measures performed on face-centered cubic structures (Dunstan and Bushby, 2014; Mu et al., 2016). The first micro-plasticity regime is followed by a second well-established plasticity regime with lower hardening slope H_2. The latter hardening slope also changes with the geometrical size h (see Fig. 3). This is clear while comparing $h = 2\,\mu\text{m}$ and $h = 10\,\mu\text{m}$. Fig. 4b shows the log-log evolution of the hardening as a function of the size h. This curve demonstrates that the hardening in the well-established plasticity regime yields as $h^{-0.5}$ scaling relationship under shearing.

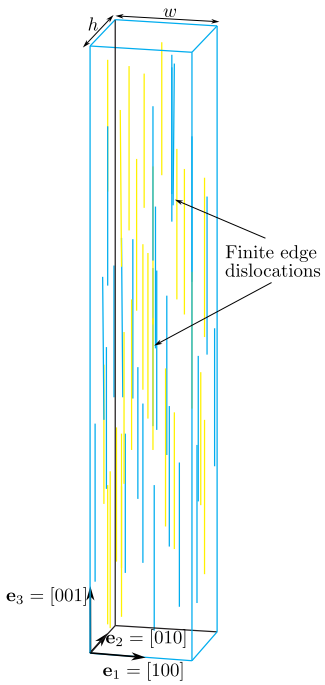

(a) 3D DDD intial configuration with finite length edge dislocations.

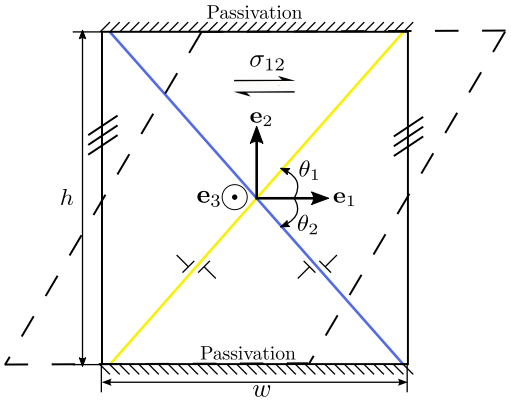

(b) Projection along $\mathbf{e}_3$: Shearing case.

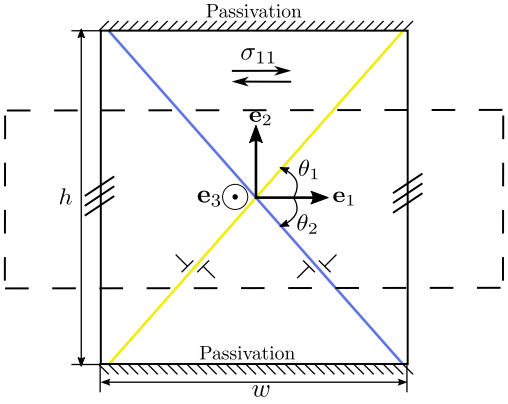

(c) Projection along $\mathbf{e}_3$: Tensile-compression case.

Fig. 1. Problem setup: double-slip configuration, solid lines correspond to initial strips and dash lines to deformed ones.

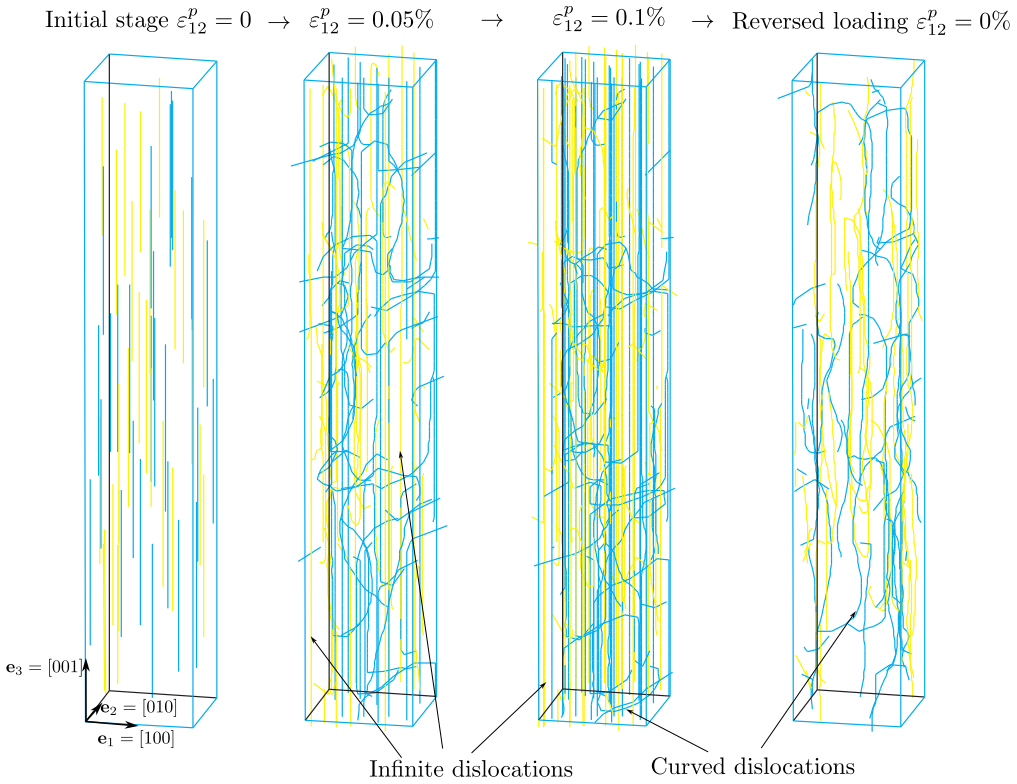

Fig. 2. Illustration of the dislocation structure during the shearing loading in the double-slip case and with passivation conditions along $\mathbf{e}_2$ and periodic boundary conditions along $\mathbf{e}_1$ and $\mathbf{e}_3$.

For the overall cyclic loading, a strong kinematic hardening effect can be outlined from these results, indicating the large dominance of kinematic hardening over isotropic hardening. As seen in several experiments (Stoltz and Pelloux, 1976; Hidayetoglu et al., 1985; Kiener et al., 2010), the curves take the form of closed loops. For these DDD simulations under shearing, inflected hysteretic behavior is obtained in the reverse loading phase (*i.e.,* $\varepsilon_{12}^p : 0.1\% \rightarrow -0.1\%$). This uncommon non-convex shape is identified as KIII kinematic hardening of Asaro (Asaro, 1975), which has been pointed out in several experimental works (Stoltz and Pelloux, 1976; Taillard and Pineau, 1982; Hidayetoglu et al., 1985; Proudhon et al., 2008; Sharma et al., 2014) in the first few cycles of cyclic loading. It corresponds to a first-in/last-out sequence of dislocation motion in the plastic recovery mechanism, since conditions for planar glide favour the reversal of dislocations along their original paths. In these simulations and experiments, the observed inflected zones are quite centered around a zero plastic strain (see Fig. 3a). Single-slip case has also been analyzed and it leads to the same conclusions as in the double-slip case. Fig. 5 shows here the example of the size $h = 2\,\mu\mathrm{m}$. The only change is a greater hardening slope in the well-established plasticity regime. Indeed, having only one slip system makes it more difficult for the dislocation structure to accommodate the loading, as GND walls rapidly form and act as barriers to dislocation movements. It is worth mentioning that the large dominance of the kinematic hardening over isotropic hardening is not a general rule. At very large initial dislocation densities, forest dislocations can generate isotropic hardening. In fact, experimental tests (*e.g.,* shearing (Tagarielli and Fleck, 2010) or torsion (Liu et al., 2013)) have demonstrated the presence of isotropic hardening to a greater or equal extent than kinematic hardening.

Size effects have also been examined under tension-compression. Fig. 6 presents the macroscopic response, where strengthening (as consequence of a micro-plasticity process) and KIII kinematic hardening of Asaro are significantly noticeable similarly to the shearing case. The apparent higher-order yield stress

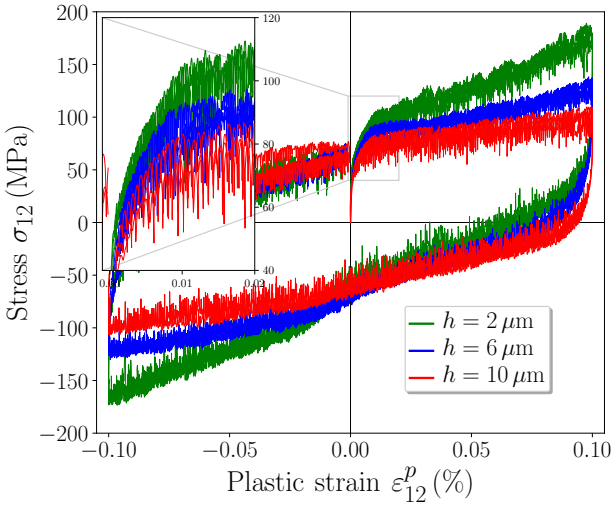

(a) Raw curves: σ_{12} as function of the plastic strain ε^p_{12}.

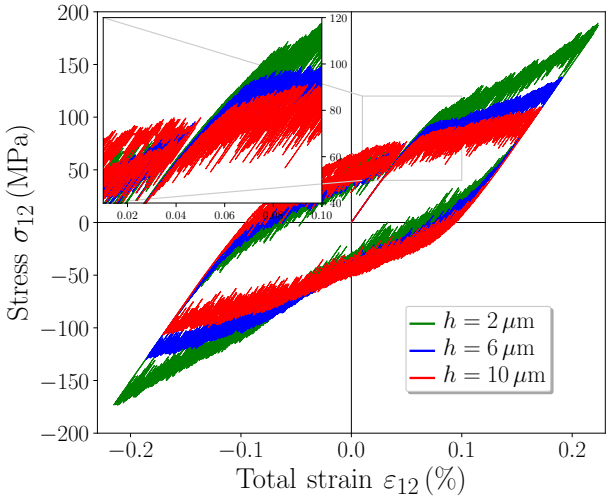

(b) Raw curves: σ_{12} as function of the total strain ε_{12}.

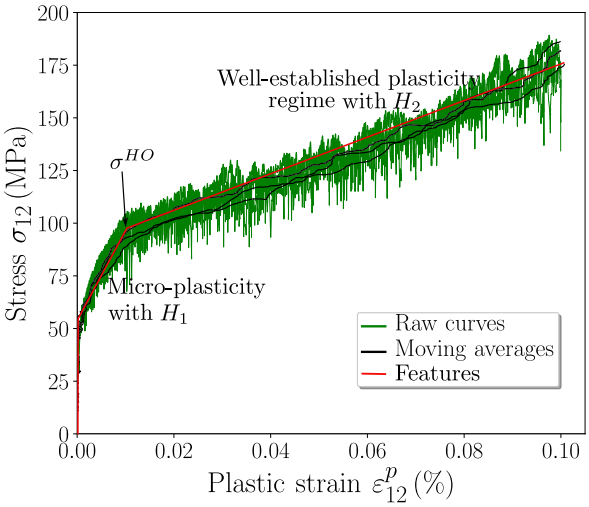

(c) Detail of the plastic activity: higher-order yield stress σ^{HO} and hardening slope H_1 and H_2 definitions (example of $h = 2\,\mu$m).

Fig. 3. Size effects in shearing with DDD: double-slip configuration with passivation; h is the geometrical size. The three different sample results are plotted. Raw curves are the ones obtained directly from the simulations.

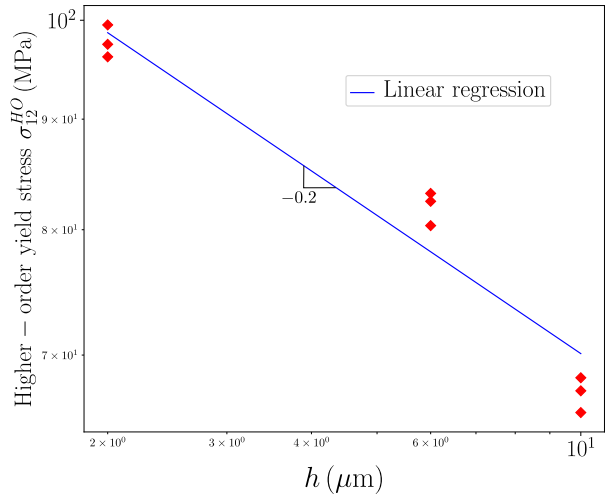

(a) Log-log apparent yield stress evolution.

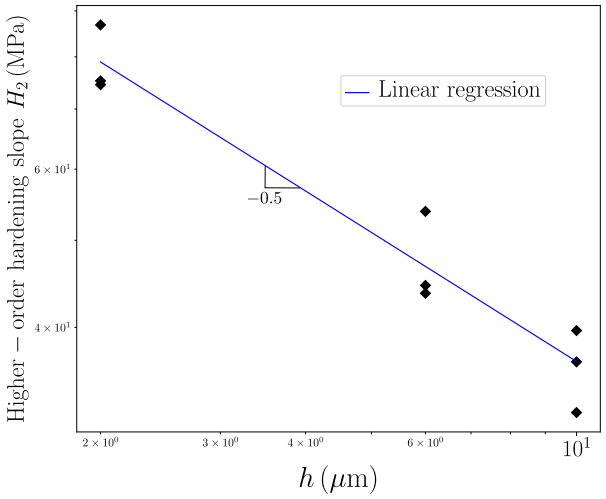

(b) Log-log hardening in the well-established plasticity regime.

Fig. 4. Stress and hardening evolutions in shearing as function of the geometrical size h. The stresses extracted for this analysis correspond to the moving average values.

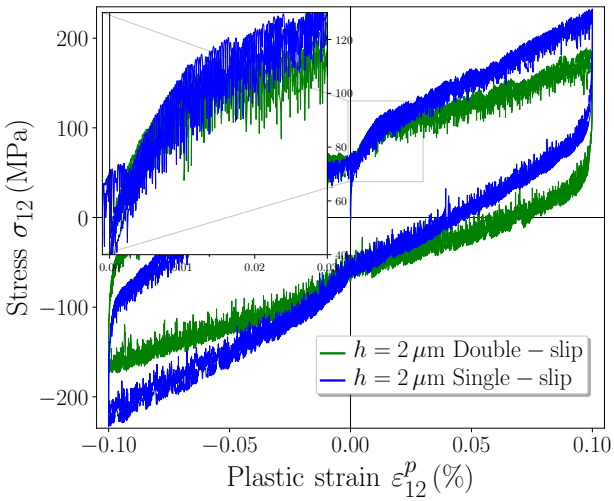

(a) σ_{12} as function of the plastic strain ε_{112}^{p}.

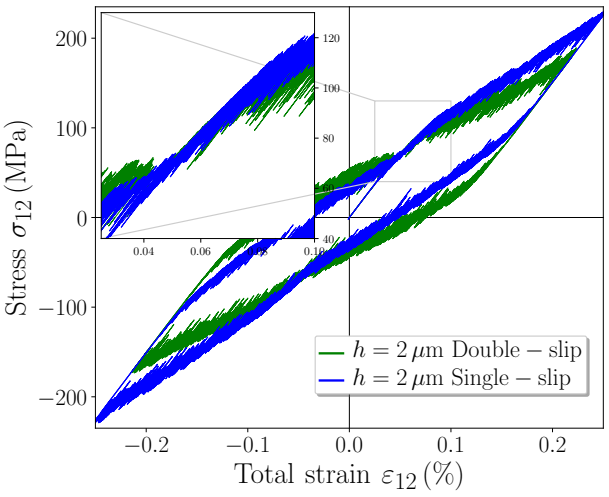

(b) σ_{12} as function of the total strain ε_{12}.

Fig. 5. Comparison between single- and double-slip in shearing with passivation.

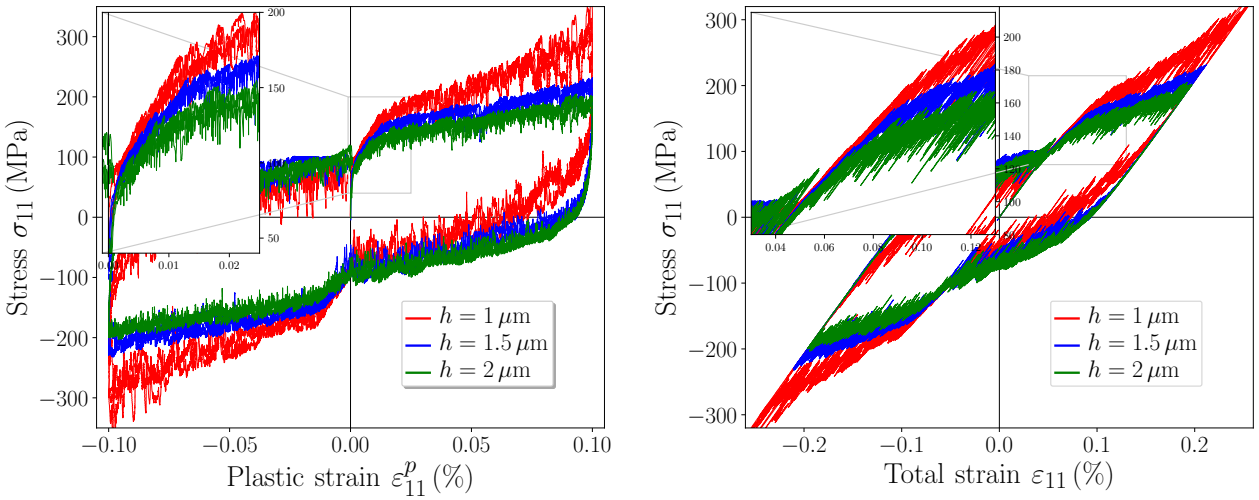

(a) σ_{11} as function of the plastic strain ε^p_{11}.

(b) σ_{11} as function of the total strain ε_{11}.

Fig. 6. Size effects in tension-compression with DDD: double-slip configuration with passivation.

in tensile case is plotted against the geometrical size h in a log-log space in Fig. 7a. Here σ^{HO}_{11} evolves as $h^{-0.3}$ scaling relationship:

$$\sigma^{HO}_{11} \propto h^{-0.3} \tag{4}$$

Fig. 7b proves that the hardening in the second plasticity regime presents $h^{-1.1}$ scaling relationship. These results demonstrate that the scaling exponent depends on the loading type. This could explain the difficulty in reaching a consensus regarding the scaling relationship in the literature (Dunstan and Bushby, 2014; Cordero et al., 2016; Stallard et al., 2023). Due to the similarity in results between cyclic shearing and tension-compression, the continuum models developed in the following section will mainly be analyzed considering the 2D shearing case. The parameters of the models are identified through DDD shearing results. A prediction and comparison for the tension-compression case will also be made based on these identified parameters.

3. Higher-order crystal plasticity models: Kinematic hardening modeling

In the previous section, a thorough examination of size effects is conducted through DDD simulations. This investigation underscores the importance of strengthening and hardening effects and their correlation with the geometrical size h. It particularly emphasizes the relevance of the KIII kinematic hardening of Asaro (Asaro, 1975) in small-scale plasticity. The current section aims at applying these findings to suggest ameliorated SGCP models, inspired by a recent model developed by the authors (Jebahi and Forest, 2023), to accurately mimic the observed phenomena.

3.1. General aspects of gradient-enhanced single-crystal continua and associated balance equations

Consider $\mathbf{u}(\mathbf{x}, t)$ as the displacement of a given material point identified by $\mathbf{x}$ at time t within a subregion $\mathcal{V}$ of the continuum under study. Within the context of small deformations, the displacement gradient $\boldsymbol{\nabla}\mathbf{u}$ can be decomposed additively in the following manner:

$$\boldsymbol{\nabla}\mathbf{u} = \mathbf{H} = \mathbf{H}_e + \mathbf{H}_p \tag{5}$$

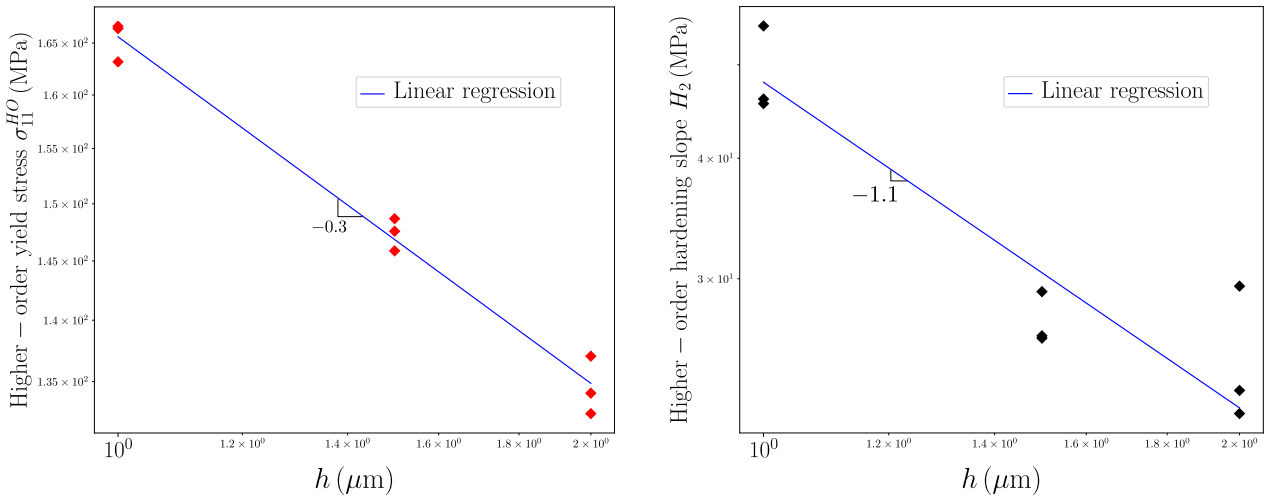

(a) Log-log apparent yield stress evolution.

(b) Log-log hardening in the well-established plasticity regime.

Fig. 7. Stress and hardening evolutions in tension-compression as function of the geometrical size h.

where $\mathbf{H}_e$ and $\mathbf{H}_p$ are respectively the elastic distortion, due to stretch and rotation of the underlying lattice, and the plastic distortion, due to plastic flow. In single-crystal plasticity, the plastic distortion tensor can be expressed as:

$$\mathbf{H}_p = \sum_{\alpha=1}^{q} \gamma^\alpha \left[\mathbf{s}^\alpha \otimes \mathbf{m}^\alpha\right] \tag{6}$$

where γ^α, $\mathbf{s}^\alpha$ and $\mathbf{m}^\alpha$ are respectively the plastic slip, the unit slip direction and the unit slip-plane normal associated with slip system α, q is the total number of slip systems in the single-crystal, and "$\otimes$" is the tensor product. The unit vector defined by $\mathbf{l}^\alpha = \mathbf{s}^\alpha \times \mathbf{m}^\alpha$ represents the line direction of dislocation distribution ("$\times$" denotes the cross product).

Following the definition of $\mathbf{H}_e$ and $\mathbf{H}_p$, their respective symmetric and skew-symmetric parts are introduced:

$$\boldsymbol{\varepsilon}_e = \frac{1}{2}\left[\mathbf{H}_e + \mathbf{H}_e^T\right],\ \boldsymbol{\varepsilon}_p = \frac{1}{2}\left[\mathbf{H}_p + \mathbf{H}_p^T\right],\ \boldsymbol{\omega}_e = \frac{1}{2}\left[\mathbf{H}_e - \mathbf{H}_e^T\right],\ \boldsymbol{\omega}_p = \frac{1}{2}\left[\mathbf{H}_p - \mathbf{H}_p^T\right] \tag{7}$$

where $\boldsymbol{\varepsilon}_e$, $\boldsymbol{\varepsilon}_p$, $\boldsymbol{\omega}_e$ and $\boldsymbol{\omega}_p$ are respectively the elastic and plastic strain tensors, and the elastic and plastic rotation tensors. Therefore, the plastic strain rate tensor $\dot{\boldsymbol{\varepsilon}}_p$ can be written as:

$$\dot{\boldsymbol{\varepsilon}}_p = \sum_{\alpha=1}^{q} \dot{\gamma}^\alpha \mathbf{P}^\alpha \tag{8}$$

with $\mathbf{P}^\alpha$ the symmetrized Schmid tensor associated with slip system α:

$$\mathbf{P}^\alpha = \frac{1}{2}\left(\mathbf{s}^\alpha \otimes \mathbf{m}^\alpha + \mathbf{m}^\alpha \otimes \mathbf{s}^\alpha\right) \tag{9}$$

In the present work on generalized continua, the traditional degrees of freedom (DOF), represented by the displacement fields $\mathbf{u}$, are expanded to include the plastic slip fields γ^α as primary variables. In order to simplify notations, the symbol $\boldsymbol{\kappa}^\alpha$ is used to denote the plastic slip gradient associated with slip system α

($\boldsymbol{\kappa}^\alpha = \boldsymbol{\nabla}\gamma^\alpha$). Assuming static case with no body forces, the power of internal and external forces can then be expressed as (Germain, 1973; Gurtin et al., 2007):

$$\begin{cases} \mathcal{P}_{int} = \displaystyle\int_{\mathcal{V}} \boldsymbol{\sigma} : \delta\dot{\boldsymbol{\varepsilon}}_e \,\mathrm{dv} + \sum_{\alpha=1}^{q} \int_{\mathcal{V}} \pi^\alpha \delta\dot{\gamma}^\alpha \,\mathrm{dv} + \sum_{\alpha=1}^{q} \int_{\mathcal{V}} \boldsymbol{\xi}^{\boldsymbol{\alpha}} \cdot \delta\dot{\boldsymbol{\kappa}}^\alpha \,\mathrm{dv} \\ \mathcal{P}_{ext} = \displaystyle\int_{\mathcal{S}} \mathbf{t} \cdot \delta\dot{\mathbf{u}} \,\mathrm{ds} + \sum_{\alpha=1}^{q} \int_{\mathcal{S}} \chi^\alpha \delta\dot{\gamma}^\alpha \,\mathrm{ds} \end{cases} \tag{10}$$

where $\boldsymbol{\sigma}$ is the classical macroscopic Cauchy stress tensor, π^α refers to a microscopic stress scalar defined on slip system α (work-conjugate to γ^α), $\boldsymbol{\xi}^\alpha$ represents a microscopic stress vector defined on slip system α (work-conjugate to $\boldsymbol{\nabla}\gamma^\alpha$), $\mathbf{t}$ is the macroscopic traction and χ^α is a microscopic traction for slip system α both acting on the boundary $\mathcal{S}$ of the considered subregion $\mathcal{V}$. Application of the virtual power principle leads to two types of balance equations and boundary conditions:

$$\begin{cases} \boldsymbol{\nabla}\cdot\boldsymbol{\sigma} &= \mathbf{0} \quad \text{in} \quad \mathcal{V} \\ \boldsymbol{\sigma}\cdot\mathbf{n} &= \mathbf{t} \quad \text{on} \quad \mathcal{S} \end{cases} \tag{11}$$

and

$$\begin{cases} \tau^\alpha + \boldsymbol{\nabla}\cdot\boldsymbol{\xi}^\alpha - \pi^\alpha &= 0 \quad \text{in} \quad \mathcal{V} \\ \boldsymbol{\xi}^\alpha \cdot \mathbf{n} &= \chi^\alpha \quad \text{on} \quad \mathcal{S} \end{cases} \tag{12}$$

with $\tau^\alpha = \boldsymbol{\sigma} : (\mathbf{s}^\alpha \otimes \mathbf{m}^\alpha)$ the resolved shear stress on slip system α and $\mathbf{n}$ the outward unit normal to $\mathcal{S}$.

To derive the associated constitutive equations within a thermodynamically-consistent framework, selecting suitable internal variables for the free energy ψ (Helmholtz free energy volume density) is crucial. Subsequently, it is necessary to apply the second law of thermodynamics (dissipation inequality), which, from a purely mechanical perspective, can be written using the assumed expressions of internal and external powers in Eq. (10) as follows:

$$\dot{\int_{\mathcal{V}} \psi \,\mathrm{dv}} \leq \mathcal{P}_{ext} = \mathcal{P}_{int} \quad \Longleftrightarrow \quad \boldsymbol{\sigma} : \dot{\boldsymbol{\varepsilon}}_e + \sum_{\alpha=1}^{q} \pi^\alpha \dot{\gamma}^\alpha + \boldsymbol{\xi}^{\boldsymbol{\alpha}} \cdot \dot{\boldsymbol{\kappa}}^\alpha - \dot{\psi} \geq 0 \tag{13}$$

3.2. A brief overview of the original SGCP model developed by Jebahi and Forest (2023)

The present subsection briefly reviews the thermodynamic aspects of the SGCP model developed by Jebahi and Forest (2023), which is used as basis for the development of the present versions. This model has been developed to address the issue of "elastic-gaps" (Fleck et al., 2014), whose physical reality is often questioned, while including higher-order dissipation. It is based on the decomposition of the plastic slip gradients $\boldsymbol{\kappa}^\alpha$ into recoverable (energetic) $\boldsymbol{\kappa}_r^\alpha$ and unrecoverable (dissipative) $\boldsymbol{\kappa}_d^\alpha$ parts:

$$\boldsymbol{\kappa}^\alpha = \boldsymbol{\kappa}_r^\alpha + \boldsymbol{\kappa}_d^\alpha \tag{14}$$

Considering this decomposition, only the recoverable parts of the plastic slip gradients $\boldsymbol{\kappa}_r^\alpha$ are considered in the free energy density:

$$\psi = \psi(\boldsymbol{\varepsilon}_e, \boldsymbol{\gamma}, \boldsymbol{\kappa}_r) \tag{15}$$

with $\boldsymbol{\gamma} = \left(\gamma^1, \gamma^2, \ldots, \gamma^q\right)$ and $\boldsymbol{\kappa}_r = \left(\boldsymbol{\kappa}_r^1, \boldsymbol{\kappa}_r^2, \ldots, \boldsymbol{\kappa}_r^q\right)$. In contrast, ψ depends on the total plastic slip gradients in classical Gurtin-type SGCP models (Gurtin et al., 2007). Using the definition in Eq. (15), the dissipation inequality (13) becomes:

$$\left(\boldsymbol{\sigma} - \frac{\partial\psi}{\partial\boldsymbol{\varepsilon}_e}\right) : \dot{\boldsymbol{\varepsilon}}_e + \sum_{\alpha=1}^{q} \left(\pi^\alpha - \frac{\partial\psi}{\partial\gamma^\alpha}\right) \dot{\gamma}^\alpha + \sum_{\alpha=1}^{q} \left(\boldsymbol{\xi}^\alpha - \frac{\partial\psi}{\partial\boldsymbol{\kappa}_r^\alpha}\right) \cdot \dot{\boldsymbol{\kappa}}_r^\alpha + \sum_{\alpha=1}^{q} \boldsymbol{\xi}^\alpha \cdot \dot{\boldsymbol{\kappa}}_d^\alpha \geq 0 \tag{16}$$

The macroscopic stress $\boldsymbol{\sigma}$ is assumed to be fully energetic:

$$\boldsymbol{\sigma} = \frac{\partial \psi}{\partial \boldsymbol{\varepsilon}_e} \tag{17}$$

and the first-order microscopic stresses can be divided into recoverable and dissipative parts:

$$\pi^\alpha = \pi_r^\alpha + \pi_d^\alpha \tag{18}$$

with the recoverable parts given by:

$$\pi_r^\alpha = \frac{\partial \psi}{\partial \gamma^\alpha} \tag{19}$$

The higher-order microscopic stresses are considered to be fully recoverable and are formulated as follows:

$$\boldsymbol{\xi}^\alpha = \frac{\partial \psi}{\partial \boldsymbol{\kappa}_r^\alpha} \tag{20}$$

Using the above constitutive assumptions, the residual dissipation (16) reduces to:

$$d^{res} = \sum_{\alpha=1}^{q} \pi_d^\alpha \, \dot{\gamma}^\alpha + \sum_{\alpha=1}^{q} \boldsymbol{\xi}^\alpha \cdot \dot{\boldsymbol{\kappa}}_d^\alpha \geq 0 \tag{21}$$

As discussed in Jebahi and Forest (2023), the control of the higher-order hardening after activation of the higher-order dissipation is only possible through the higher-order isotropic hardening parameters. Consequently, cyclic loading invariably leads to open macroscopic response loops (unlimited cyclic hardening). However, this contradicts the findings from DDD simulations, where dominating kinematic hardening effects with nearly closed loops are observed under cyclic loading, as demonstrated in Figs. 3, 5, and 6. Further improvements are then needed to better consider higher-order kinematic effects. In the next subsections, two ways to address this need are proposed.

3.3. Proposed SGCP models with advanced description of higher-order kinematic effects

In this section, two approaches are suggested to better consider higher-order kinematic hardening effects within SGCP theories, based on Prager-type and Chaboche-type (multi-kinematic) formulations.

3.3.1. Prager-type formulation

In contrast to the prior framework proposed in Jebahi and Forest (2023), the total free energy density ψ given by (15) is enriched by explicitly considering the unrecoverable parts of the plastic slip gradients $\boldsymbol{\kappa}_d^\alpha$ in its formulation:

$$\psi = \psi\left(\boldsymbol{\varepsilon}_e,\, \boldsymbol{\gamma},\, \boldsymbol{\kappa}_r,\, \boldsymbol{\kappa}_d\right) \tag{22}$$

Adding $\boldsymbol{\kappa}_d^\alpha$ as an argument for the free energy may be regarded as an expression of dissipative hardening rule via an energetic approach (Simo and Hughes, 1999; Gurtin and Reddy, 2009; Xiao et al., 2012). This ensures that the hardening behavior aligns with the fundamental principles of thermodynamics. Using this expression, the dissipation inequality (13) becomes:

$$\left(\boldsymbol{\sigma} - \frac{\partial \psi}{\partial \boldsymbol{\varepsilon}_e}\right) : \dot{\boldsymbol{\varepsilon}}_e + \sum_{\alpha=1}^{q} \left(\pi^\alpha - \frac{\partial \psi}{\partial \gamma^\alpha}\right) \dot{\gamma}^\alpha + \sum_{\alpha=1}^{q} \left(\boldsymbol{\xi}^\alpha - \frac{\partial \psi}{\partial \boldsymbol{\kappa}_r^\alpha}\right) \cdot \dot{\boldsymbol{\kappa}}_r^\alpha + \sum_{\alpha=1}^{q} \left(\boldsymbol{\xi}^\alpha - \frac{\partial \psi}{\partial \boldsymbol{\kappa}_d^\alpha}\right) \cdot \dot{\boldsymbol{\kappa}}_d^\alpha \geq 0 \tag{23}$$

with Eqs. (17), (18), (19) and (20) remain valid. It follows that the residual dissipation can be written as:

$$d^{res} = \sum_{\alpha=1}^{q} \pi_d^\alpha \, \dot{\gamma}^\alpha + \sum_{\alpha=1}^{q} (\boldsymbol{\xi}^\alpha - \mathbf{X}^\alpha) \cdot \dot{\boldsymbol{\kappa}}_d^\alpha \geq 0 \tag{24}$$

where $\mathbf{X}^\alpha$ is a Prager-like higher-order backstress defined on slip system α by:

$$\mathbf{X}^\alpha = \frac{\partial \psi}{\partial \boldsymbol{\kappa}_d^\alpha} \tag{25}$$

Note that the term $(\boldsymbol{\xi}^\alpha - \mathbf{X}^\alpha)$ characterizes the effective higher-order stress associated with the evolution of dislocations on the slip plane α. Since the motion direction of these dislocations is tangent to this plane, this term is also required to be tangential. In this work, both $\boldsymbol{\xi}^\alpha$ and $\mathbf{X}^\alpha$ are considered to be tangent to the slip plane α. As in Jebahi et al. (2020) and Jebahi and Forest (2023), the first- and higher-order dissipative effects are assumed to be uncoupled and described using independent effective plastic slip measures. This gives the possibility to treat the two terms of (24) separately.

The positivity of the first-order dissipation ($\pi_d^\alpha \, \dot{\gamma}^\alpha \geq 0$) is ensured by using a description of the first-order dissipative stresses in a rate-dependent formulation identical to the one used in Jebahi and Forest (2023):

$$\pi_d^\alpha = S_\pi^\alpha \left[\frac{\dot{e}_\pi^\alpha}{\dot{\gamma}_0^\alpha} \right]^m \frac{\dot{\gamma}^\alpha}{\dot{e}_\pi^\alpha} \quad \text{with} \quad \dot{e}_\pi^\alpha = |\dot{\gamma}^\alpha| \tag{26}$$

where $\dot{\gamma}_0^\alpha > 0$ is a constant reference strain rate representative of the flow rates of interest, $m > 0$ is a constant characterizing the rate-sensitivity of the considered material and $S_\pi^\alpha > 0$ is a stress-dimensional slip resistance associated with slip system α, referred to hereafter as first-order slip resistance. To model first-order isotropic hardening, the latter variable is assumed to evolve according to:

$$\dot{S}_\pi^\alpha = \sum_{\beta=1}^{q} H_\pi \, \dot{e}_\pi^\beta \quad \text{with} \quad S_\pi^\alpha(0) = S_{\pi 0} > 0, \; H_\pi = \text{constant} \geq 0 \tag{27}$$

with H_π first-order (isotropic-like) hardening modulus. The reader is referred to the work of Gurtin et al. (2007) for more general hardening formulations.

To ensure the non-negativity of the higher-order dissipation (*i.e.,* $[\boldsymbol{\xi}^\alpha - \mathbf{X}^\alpha] \cdot \dot{\boldsymbol{\kappa}}_d^\alpha \geq 0$), the same methodology proposed by Jebahi and Forest (2023) within rate-dependent framework is used in the present study. The higher-order dissipation is modeled by constraining the evolution of the equivalent higher-order stresses, which are expressed for each slip system α as (note that $\boldsymbol{\xi}^\alpha$ and $\mathbf{X}^\alpha$ are tangent to the slip plane α):

$$\xi_{eq}^\alpha = \sqrt{(\mathbf{s}^\alpha \cdot [\boldsymbol{\xi}^\alpha - \mathbf{X}^\alpha])^2 + (\mathbf{l}^\alpha \cdot [\boldsymbol{\xi}^\alpha - \mathbf{X}^\alpha])^2} = \|\boldsymbol{\xi}^\alpha - \mathbf{X}^\alpha\| \tag{28}$$

As in Jebahi and Forest (2023), ξ_{eq}^α is assumed to be governed by a rate-dependent constitutive equation as follows:

$$\xi_{eq}^\alpha = S_\xi^\alpha \, l_d \left[\frac{\dot{\kappa}_d^\alpha}{\dot{\gamma}_0^\alpha} \right]^m \quad \text{with} \quad \dot{\kappa}_d^\alpha = \|l_d \, \dot{\boldsymbol{\kappa}}_d^\alpha\| \tag{29}$$

where $S_\xi^\alpha \geq 0$ is a stress-dimensional slip resistance associated with the slip system α, referred to hereafter as higher-order dissipative slip resistance, and l_d is a dissipative length scale. In a manner analogous to the evolution of the first-order slip resistance, S_ξ^α is governed for each slip system α by:

$$\dot{S}_\xi^\alpha = \sum_{\beta=1}^{q} H_\xi \, \dot{\kappa}_d^\beta \quad \text{with} \quad S_\xi^\alpha(0) = S_{\xi 0} > 0, \; H_\xi = \text{constant} \geq 0 \tag{30}$$

with H_ξ representing higher-order (isotropic-like) hardening modulus. For each slip system α, the dissipative part of the plastic strain gradient rate $\dot{\boldsymbol{\kappa}}_d^\alpha$ is linked to the effective higher-order stress $(\boldsymbol{\xi}^\alpha - \mathbf{X}^\alpha)$ through a normality-like flow rule:

$$\dot{\boldsymbol{\kappa}}_d^\alpha = \frac{\dot{\kappa}_d^\alpha}{l_d} \frac{\boldsymbol{\xi}^\alpha - \mathbf{X}^\alpha}{\xi_{eq}^\alpha} \tag{31}$$

Using the above expression, it can easily be verified that higher-order dissipation, which is represented by $(\boldsymbol{\xi}^\alpha - \mathbf{X}^\alpha) \cdot \dot{\boldsymbol{\kappa}}_d^\alpha$, is always non-negative.

To complete the constitutive relations for the stresses presented in the macroscopic and microscopic balance equations, it is necessary to make explicit the form of the total Helmholtz free energy density (22). This density is assumed to be the sum of a classical elastic energy density ψ_e and a defect energy density ψ_p. Classical quadratic form in $\boldsymbol{\varepsilon}_e$ is assumed for ψ_e:

$$\psi_e = \frac{1}{2} \boldsymbol{\varepsilon}_e : \mathbb{C} : \boldsymbol{\varepsilon}_e \tag{32}$$

where $\mathbb{C}$ denotes the symmetric positive-definite elasticity tensor. Regarding the defect energy density ψ_p, an enriched power-law form, inspired by Jebahi and Forest (2023), is proposed in this work:

$$\psi_p \;=\; \frac{1}{n} X_0 \, l_{en}^n \sum_{\alpha=1}^{q} \left[\left| \varrho_{\vdash}^\alpha \right|^n + \left| \varrho_{\odot}^\alpha \right|^n \right] \;+\; \frac{1}{2} H_p \, l_d^2 \, \boldsymbol{\kappa}_d^\alpha \cdot \boldsymbol{\kappa}_d^\alpha \tag{33}$$

where X_0 is a constant representing the higher-order energetic (non-dissipative) slip resistance, l_{en} is an energetic length scale, n is an adjustable order-controlling exponent ($n \geq 1$ in order to ensure the convexity of ψ_p), H_p is a higher-order Prager-type hardening parameter. The quantities $\varrho_{\vdash}^\alpha$ and $\varrho_{\odot}^\alpha$ are introduced in Jebahi and Forest (2023) as recoverable parts of the edge and screw GND densities associated with slip system α, respectively. Inspired by Arsenlis and Parks (1999), they are derived from the recoverable parts of the plastic slip gradients as:

$$\varrho_{\vdash}^\alpha = -\mathbf{s}^\alpha \cdot \boldsymbol{\kappa}_r^\alpha \quad , \quad \varrho_{\odot}^\alpha = \mathbf{l}^\alpha \cdot \boldsymbol{\kappa}_r^\alpha \tag{34}$$

The power-law form assumed for the first part of the defect energy density is extensively documented in gradient-enhanced crystal plasticity (Bardella and Panteghini, 2015; Bayerschen and Böhlke, 2016; Panteghini et al., 2019). The specific case of $n = 1$ corresponds to the so-called rank-one model, in which the defect energy evolves linearly with the GND densities. This particular form can be justified by simple line tension arguments, as discussed in Ohno and Okumura (2007) and Wulfinghoff et al. (2015). It is worth noting that logarithmic-type forms are also widely used to express the defect energy ψ_p (Kooiman et al., 2015; Wulfinghoff et al., 2015; Lee and Schulz, 2023). Inverse functions, $\sinh^{-1}$ and $\tanh^{-1}$, have also been used as well for ψ_p (Zecevic et al., 2023). The non-quadratic power-law and logarithmic forms have shown their capability to model the KIII kinematic hardening of Asaro (Wulfinghoff et al., 2015; El-Naaman et al., 2019; Jebahi et al., 2020; Jebahi and Forest, 2023). Considering Eqs. (32) and (33), the total free energy density ψ can be rewritten, in a more detailed form, as:

$$\psi\left(\boldsymbol{\varepsilon}_e, \boldsymbol{\gamma}, \boldsymbol{\kappa}_r, \boldsymbol{\kappa}_d\right) = \frac{1}{2} \boldsymbol{\varepsilon}_e : \mathbb{C} : \boldsymbol{\varepsilon}_e + \frac{1}{n} X_0 \, l_{en}^n \sum_{\alpha=1}^{q} \left[\left| \mathbf{s}^\alpha \cdot \boldsymbol{\kappa}_r^\alpha \right|^n + \left| \mathbf{l}^\alpha \cdot \boldsymbol{\kappa}_r^\alpha \right|^n \right] + \frac{1}{2} H_p \, l_d^2 \, \boldsymbol{\kappa}_d^\alpha \cdot \boldsymbol{\kappa}_d^\alpha \tag{35}$$

Using this expression, the constitutive laws governing the energetic (non-dissipative) stresses involved in the

proposed Prager-type model can be derived:

$$\begin{cases} \boldsymbol{\sigma} = \dfrac{\partial \psi}{\partial \boldsymbol{\varepsilon}_e} = \mathbb{C} : \boldsymbol{\varepsilon}_e \\ \pi_r^\alpha = \dfrac{\partial \psi}{\partial \gamma^\alpha} = 0 \\ \boldsymbol{\xi}^\alpha = \dfrac{\partial \psi}{\partial \boldsymbol{\kappa}_r^\alpha} = X_0 \, l_{en}^n \left[|\mathbf{s}^\alpha \cdot \boldsymbol{\kappa}_r^\alpha|^{n-2} \, \mathbf{s}^\alpha \otimes \mathbf{s}^\alpha + |\mathbf{l}^\alpha \cdot \boldsymbol{\kappa}_r^\alpha|^{n-2} \, \mathbf{l}^\alpha \otimes \mathbf{l}^\alpha \right] \cdot \boldsymbol{\kappa}_r^\alpha \\ \mathbf{X}^\alpha = \dfrac{\partial \psi}{\partial \boldsymbol{\kappa}_d^\alpha} = H_p l_d^2 \, \boldsymbol{\kappa}_d^\alpha \end{cases} \tag{36}$$

Note that the obtained form of the higher-order Prager backstress $\mathbf{X}^\alpha$ echoes the Prager stress in conventional plasticity with the form of $\mathbf{X} = (2/3) \, H \, \boldsymbol{\varepsilon}_p$ (Besson et al., 2010). Considering these expressions, the overall constitutive equations associated with the Prager-type model can be summarized as follows:

$$\begin{cases} \dot{\boldsymbol{\sigma}} = \mathbb{C} : \dot{\boldsymbol{\varepsilon}}_e \\ \dot{\pi}_r^\alpha = 0 \\ \dot{\boldsymbol{\xi}}^\alpha = \mathbf{A}^{\alpha\alpha} \cdot \boldsymbol{\kappa}_r^\alpha \quad \text{with} \quad \mathbf{A}^{\alpha\alpha} = (n-1) \, X_0 \, l_{en}^n \left[|\mathbf{s}^\alpha \cdot \boldsymbol{\kappa}_r^\alpha|^{n-2} \, \mathbf{s}^\alpha \otimes \mathbf{s}^\alpha + |\mathbf{l}^\alpha \cdot \boldsymbol{\kappa}_r^\alpha|^{n-2} \, \mathbf{l}^\alpha \otimes \mathbf{l}^\alpha \right] \\ \pi_d^\alpha = S_\pi^\alpha \left[\dfrac{\dot{e}_\pi^\alpha}{\dot{\gamma}_0^\alpha} \right]^m \dfrac{\dot{\gamma}^\alpha}{\dot{e}_\pi^\alpha} \quad \text{with} \quad \dot{e}_\pi^\alpha = |\dot{\gamma}^\alpha| \\ \dot{S}_\pi^\alpha = \displaystyle\sum_{\beta=1}^{q} H_\pi \, \dot{e}_\pi^\beta \quad \text{with} \quad S_\pi^\alpha(0) = S_{\pi 0} > 0, \; H_\pi = \text{constant} \geq 0 \\ \xi_{eq}^\alpha = S_\xi^\alpha \, l_d \left[\dfrac{\dot{\kappa}_d^\alpha}{\dot{\gamma}_0^\alpha} \right]^m \quad \text{with} \quad \dot{\kappa}_d^\alpha = \| l_d \, \dot{\boldsymbol{\kappa}}_d^\alpha \| \\ \dot{S}_\xi^\alpha = \displaystyle\sum_{\beta=1}^{q} H_\xi \, \dot{\kappa}_d^\beta \quad \text{with} \quad S_\xi^\alpha(0) = S_{\xi 0} > 0, \; H_\xi = \text{constant} \geq 0 \\ \mathbf{X}^\alpha = \dfrac{\partial \psi}{\partial \boldsymbol{\kappa}_d^\alpha} = H_p l_d^2 \, \boldsymbol{\kappa}_d^\alpha \\ \dot{\boldsymbol{\kappa}}_d^\alpha = \dfrac{\dot{\kappa}_d^\alpha}{l_d} \dfrac{\boldsymbol{\xi}^\alpha - \mathbf{X}^\alpha}{\xi_{eq}^\alpha} \end{cases} \tag{37}$$

These equations are integrated at the Gauss points using local backward Euler scheme (see Alg. 1 in Appendix B). Determination of the associated Jacobian matrix is detailed in Appendix C.

3.3.2. Chaboche-type (multi-kinematic) formulation

The previous subsection presents the modeling of the higher-order kinematic hardening through a Prager-type approach. In the current subsection, a Chaboche-type non-linear approach (Chaboche, 1989; Besson et al., 2010; Panteghini et al., 2019) is used to model the higher-order kinematic hardening. The present model is a more general extension of the original model of Jebahi and Forest (2023).

The microscopic balance equation $(12)_1$ can be rewritten as follows:

$$\tau^\alpha - (-\boldsymbol{\nabla} \cdot \boldsymbol{\xi}^\alpha) = \pi^\alpha \tag{38}$$

where the term $(-\boldsymbol{\nabla}\cdot\boldsymbol{\xi}^\alpha)$ generates Bauschinger-like higher-order hardening effects. In accordance with Chaboche kinematic hardening modeling, multiple kinematic variables can be superimposed, each of them being independent (Chaboche, 1989; Besson et al., 2010; Panteghini et al., 2019):

$$-\boldsymbol{\nabla}\cdot\boldsymbol{\xi}^\alpha = \mathbf{Z}^\alpha = \sum_{i=1}^{M} \mathbf{Z}_i^\alpha \tag{39}$$

where M is the total number of kinematic hardening variables associated with higher-order plastic activity. For this purpose, multiple series decompositions are introduced:

$$\begin{cases} \boldsymbol{\nabla}\gamma^\alpha = \boldsymbol{\kappa}^\alpha = \boldsymbol{\kappa}_r^{\alpha\, i} + \boldsymbol{\kappa}_d^{\alpha\, i} \quad , \quad i = [\![1, M]\!] \\ \boldsymbol{\xi}^\alpha = \displaystyle\sum_{i=1}^{M} \boldsymbol{\xi}_i^\alpha \end{cases} \tag{40}$$

Note that the specific case of $M = 1$ leads to the original model of Jebahi and Forest (2023). The general approach consists in taking $M \geq 2$ with the series decompositions in Eq. $(40)_1$ being independent.

Inspired by (15), the free energy can be expressed as a function of the elastic strain tensor $\boldsymbol{\varepsilon}_e$, the plastic slip γ^α and the recoverable parts of the plastic gradients $\boldsymbol{\kappa}_r^{\alpha\, i}$ for all the slip system α and all the decomposition i:

$$\psi = \psi(\boldsymbol{\varepsilon}_e, \gamma^\alpha, \boldsymbol{\kappa}_r^{\alpha\, i}) \quad , \quad i = [\![1, M]\!] \tag{41}$$

Using this expression, the dissipation inequality follows as:

$$d = \left(\boldsymbol{\sigma} - \frac{\partial\psi}{\partial\boldsymbol{\varepsilon}_e}\right) : \dot{\boldsymbol{\varepsilon}}_e + \sum_{\alpha=1}^{q}\left(\pi^\alpha - \frac{\partial\psi}{\partial\gamma^\alpha}\right)\dot{\gamma}^\alpha + \sum_{\alpha=1}^{q} \boldsymbol{\xi}^\alpha\cdot\dot{\boldsymbol{\kappa}}^\alpha - \sum_{\alpha=1}^{q}\sum_{i=1}^{M} \frac{\partial\psi}{\partial\boldsymbol{\kappa}_r^{\alpha\, i}}\cdot\dot{\boldsymbol{\kappa}}_r^{\alpha\, i} \geq 0 \tag{42}$$

Introducing Eq. $(40)_2$ in (42), the local dissipation d is rewritten:

$$d = \left(\boldsymbol{\sigma} - \frac{\partial\psi}{\partial\boldsymbol{\varepsilon}_e}\right) : \dot{\boldsymbol{\varepsilon}}_e + \sum_{\alpha=1}^{q}\left(\pi^\alpha - \frac{\partial\psi}{\partial\gamma^\alpha}\right)\dot{\gamma}^\alpha + \sum_{\alpha=1}^{q}\sum_{i=1}^{M}\left(\boldsymbol{\xi}_i^\alpha - \frac{\partial\psi}{\partial\boldsymbol{\kappa}_r^{\alpha\, i}}\right)\cdot\dot{\boldsymbol{\kappa}}_r^{\alpha\, i} + \sum_{\alpha=1}^{q}\sum_{i=1}^{M}\boldsymbol{\xi}_i^\alpha\cdot\dot{\boldsymbol{\kappa}}_d^{\alpha\, i} \geq 0 \tag{43}$$

The following state laws are adopted:

$$\begin{cases} \boldsymbol{\sigma} = \dfrac{\partial\psi}{\partial\boldsymbol{\varepsilon}_e} \\ \pi^\alpha = \dfrac{\partial\psi}{\partial\gamma^\alpha} + \pi_d^\alpha = \pi_r^\alpha + \pi_d^\alpha \\ \boldsymbol{\xi}_i^\alpha = \dfrac{\partial\psi}{\partial\boldsymbol{\kappa}_r^{\alpha\, i}} \end{cases} \tag{44}$$

so that the residual dissipation yields:

$$d^{res} = \sum_{\alpha=1}^{q}\pi_d^\alpha\dot{\gamma}^\alpha + \sum_{\alpha=1}^{q}\sum_{i=1}^{M}\boldsymbol{\xi}_i^\alpha\cdot\dot{\boldsymbol{\kappa}}_d^{\alpha\, i} \geq 0 \tag{45}$$

Comparing this inequality to the one obtained with the Prager-type model in (24), the first-order part of the residual dissipation is unchanged, while the higher-order parts $\boldsymbol{\xi}_i^\alpha\cdot\dot{\boldsymbol{\kappa}}_d^{\alpha\, i}$ replace $(\boldsymbol{\xi}^\alpha - \mathbf{X}^\alpha)\cdot\dot{\boldsymbol{\kappa}}_d^\alpha$. Similarly to the Prager-type model, every $\boldsymbol{\xi}_i^\alpha$ is considered to be tangential.

The non-negativity of the first-order dissipation ($\pi_d^\alpha\,\dot\gamma^\alpha \geq 0$) is treated exactly like in the Prager-type model by using the rate-dependent constitutive equations:

$$\pi_d^\alpha = S_\pi^\alpha \left[\frac{\dot e_\pi^\alpha}{\dot\gamma_0^\alpha}\right]^m \frac{\dot\gamma^\alpha}{\dot e_\pi^\alpha} \quad \text{with} \quad \dot e_\pi^\alpha = |\dot\gamma^\alpha| \tag{46}$$

S_π^α evolves following Eq. (27).

To ensure non-negative higher-order dissipation (*i.e.*, $\boldsymbol{\xi}_i^\alpha \cdot \dot{\boldsymbol{\kappa}}_d^{\alpha\,i} \geq 0$), the rate-dependent formulation is used similarly to the adopted one in the Prager-type model. As all $\boldsymbol{\xi}_i^\alpha$ are tangent to the slip plane α, the equivalent higher-order stresses $\xi_{i\,eq}^\alpha$ are written as:

$$\xi_{i\,eq}^\alpha = \sqrt{\left(\mathbf{s}^\alpha \cdot \boldsymbol{\xi}_i^\alpha\right)^2 + \left(\mathbf{l}^\alpha \cdot \boldsymbol{\xi}_i^\alpha\right)^2} = \|\boldsymbol{\xi}_i^\alpha\| \tag{47}$$

$\xi_{i\,eq}^\alpha$ is considered in a rate-dependent form as follows:

$$\xi_{i\,eq}^\alpha = S_{\xi_i}^\alpha\, l_d \left[\frac{\dot\kappa_d^{\alpha\,i}}{\dot\gamma_0^\alpha}\right]^m \quad \text{with} \quad \dot\kappa_d^{\alpha\,i} = \left\|l_d\,\dot{\boldsymbol{\kappa}}_d^{\alpha\,i}\right\| \tag{48}$$

where $S_{\xi_i}^\alpha \geq 0$ is a stress-dimensional slip resistance associated with slip system α in the decomposition i. Its rate evolves in the same manner as in Eq. (30). The dissipative part of the plastic strain gradient rate for a given slip system α and a decomposition i is expressed with a normality-like flow rule:

$$\dot{\boldsymbol{\kappa}}_d^{\alpha\,i} = \frac{\dot\kappa_d^{\alpha\,i}}{l_d}\,\frac{\boldsymbol{\xi}_i^\alpha}{\xi_{i\,eq}^\alpha} \tag{49}$$

It is essential to detail the expression of the Helmoholtz free energy to close the constitutive model. The elastic part of this energy ψ_e is kept in its classical form (see Eq. (32)), while the defect energy ψ_p is a superimposition of multiple higher-order variables:

$$\psi_p(\gamma^\alpha, \boldsymbol{\kappa}_r^{\alpha\,i}) = \sum_{i=1}^{M} \frac{1}{n_i} X_0\, l_{eni}^{n_i} \sum_{\alpha=1}^{q} \left(\left|\mathbf{s}^\alpha \cdot \boldsymbol{\kappa}_r^{\alpha\,i}\right|^{n_i} + \left|\mathbf{l}^\alpha \cdot \boldsymbol{\kappa}_r^{\alpha\,i}\right|^{n_i} \right) = \sum_{i=1}^{M} \psi_p^i(\gamma^\alpha, \boldsymbol{\kappa}_r^{\alpha\,i}) \tag{50}$$

where l_{eni} and n_i are respectively an energetic length scale and an adjustable order-controlling exponent associated with the i-th higher-order decomposition. The resulting governing laws are as follows:

$$\begin{cases}
\dot{\boldsymbol{\sigma}} = \mathbb{C} : \dot{\boldsymbol{\varepsilon}}_e \\
\dot\pi_r^\alpha = 0 \\
\dot{\boldsymbol{\xi}}_i^\alpha = \mathbf{A}_i^{\alpha\alpha} \cdot \boldsymbol{\kappa}_r^{\alpha\,i} \quad \text{with} \quad \mathbf{A}_i^{\alpha\alpha} = (n_i - 1)\, X_0\, l_{en}^{n_i} \left[\left|\mathbf{s}^\alpha \cdot \boldsymbol{\kappa}_r^{\alpha\,i}\right|^{n_i-2} \mathbf{s}^\alpha \otimes \mathbf{s}^\alpha + \left|\mathbf{l}^\alpha \cdot \boldsymbol{\kappa}_r^{\alpha\,i}\right|^{n_i-2} \mathbf{l}^\alpha \otimes \mathbf{l}^\alpha\right] \\
\pi_d^\alpha = S_\pi^\alpha \left[\dfrac{\dot e_\pi^\alpha}{\dot\gamma_0^\alpha}\right]^m \dfrac{\dot\gamma^\alpha}{\dot e_\pi^\alpha} \quad \text{with} \quad \dot e_\pi^\alpha = |\dot\gamma^\alpha| \\
\dot S_\pi^\alpha = \displaystyle\sum_{\beta=1}^{q} H_\pi\, \dot e_\pi^\beta \quad \text{with} \quad S_\pi^\alpha(0) = S_{\pi 0} > 0,\ H_\pi = \text{constant} \geq 0 \\
\xi_{i\,eq}^\alpha = S_{\xi_i}^\alpha\, l_d \left[\dfrac{\dot\kappa_d^{\alpha\,i}}{\dot\gamma_0^\alpha}\right]^m \quad \text{with} \quad \dot\kappa_d^{\alpha\,i} = \left\|l_d\,\dot{\boldsymbol{\kappa}}_d^{\alpha\,i}\right\| \\
\dot S_{\xi_i}^\alpha = \displaystyle\sum_{\beta=1}^{q} H_{\xi_i}\, \dot\kappa_d^{\beta\,i} \quad \text{with} \quad S_{\xi_i}^\alpha(0) = S_{\xi_i 0} > 0,\ H_{\xi_i} = \text{constant} \geq 0 \\
\dot{\boldsymbol{\kappa}}_d^{\alpha\,i} = \dfrac{\dot\kappa_d^{\alpha\,i}}{l_d}\,\dfrac{\boldsymbol{\xi}_i^\alpha}{\xi_{i\,eq}^\alpha}
\end{cases}$$

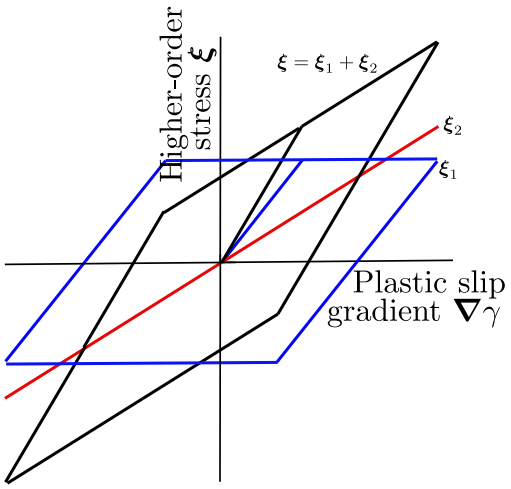

Fig. 8. Illustration of the evolution of $\boldsymbol{\xi}$ for $n_1 = n_2 = 2$ as a function of the gradient of the plastic slip $\boldsymbol{\nabla}\gamma$.

Tab. 2. Material parameters used for the SGCP simulations.

Material parameter name	Symbol	Value	Unit
Shear modulus	μ	75200	MPa
Reference slip rate	$\dot{\gamma}_0^\alpha$	0.01	s^{-1}
Rate-sensitivity parameter	m	0.01	–
Higher-order energetic slip resistance	$X_0 = \mu$	75200	MPa
Initial first-order dissipative slip resistance	$S_{\pi 0} = \tau_{\mathrm{Peierls}}$	37.6	MPa

(51)

This system is integrated at the Gauss points using an Euler backward scheme quite similar to the one in the Prager-type formation. In the scope of this work (*i.e.,* enriching SGCP capacities to describe small-scale phenomena by assimilating insights gleaned from DDD simulations), the multi-kinematic formulation is implemented with $M = 2$. Indeed, as previously stated, strengthening and hardening effects result from a two-stage plastic behavior, which can be reproduced by assuming two series decompositions. In this case, $\boldsymbol{\kappa}^\alpha$ and $\boldsymbol{\xi}^\alpha$ can be expressed:

$$\begin{cases} \boldsymbol{\kappa}^\alpha = \boldsymbol{\kappa}_r^{\alpha\,1} + \boldsymbol{\kappa}_d^{\alpha\,1} = \boldsymbol{\kappa}_r^{\alpha\,2} + \boldsymbol{\kappa}_d^{\alpha\,2} \\ \boldsymbol{\xi}^\alpha = \boldsymbol{\xi}_1^\alpha + \boldsymbol{\xi}_2^\alpha = \dfrac{\partial \psi_p^1}{\partial \boldsymbol{\kappa}_r^{\alpha\,1}} + \dfrac{\partial \psi_p^2}{\partial \boldsymbol{\kappa}_r^{\alpha\,2}} \end{cases} \tag{52}$$

$\boldsymbol{\xi}_1^\alpha$ will be considered as saturating at $S_{\xi_1 0}$ and no saturation condition will be used for $\boldsymbol{\xi}_2^\alpha$ (*i.e.,* infinite $S_{\xi_2 0}$). Fig. 8 shows an illustration of the evolution of $\boldsymbol{\xi} = \boldsymbol{\xi}_1 + \boldsymbol{\xi}_2$ for double quadratic case $n_1 = n_2 = 2$. It is important to note that methodology employed in this study is minimalistic, utilizing more complex (non-quadratic) defect energy functions. Instead of relying on numerous simple defect energy functions, as proposed in Panteghini et al. (2019), the nonlinear effects are incorporated into these functions.

4. Finite element numerical implementation and validation: 2D problem

The proposed models have been implemented using finite element method (FEM) within ABAQUS/Standard. The implementation procedure is detailed in Appendix A. To validate some aspects of the numerical implementation and to facilitate the identification of some associated parameters of the models, a simplified version

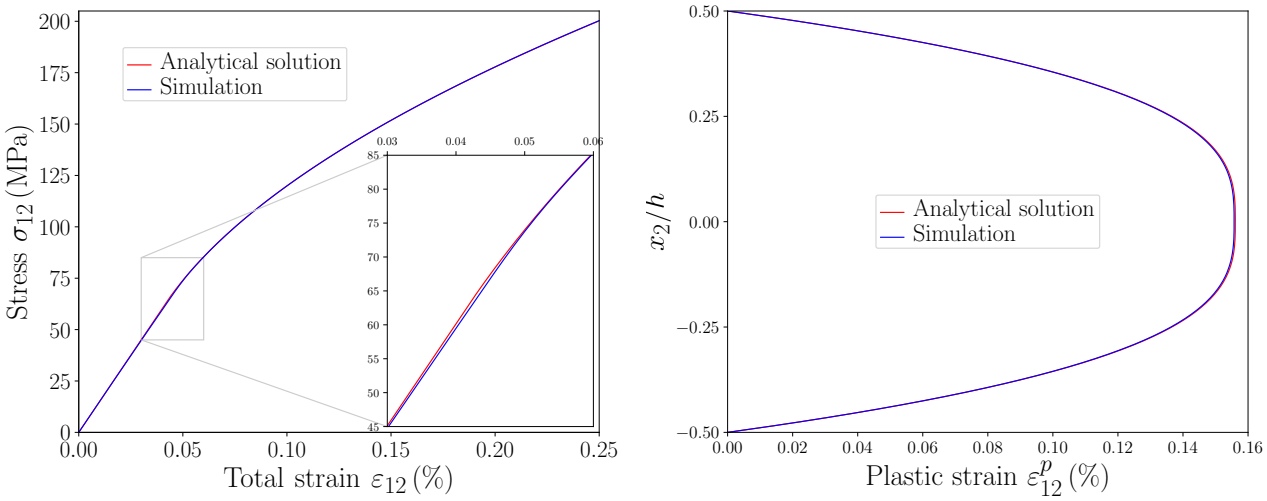

(a) Stress-Strain curves.

(b) Plastic strain profile along $\mathbf{e}_2$ direction at $\varepsilon_{12} = 0.25\%$.

Fig. 9. Example of comparison of the analytical solution with the simulation in the non-quadratic case ($n = 1.5$).

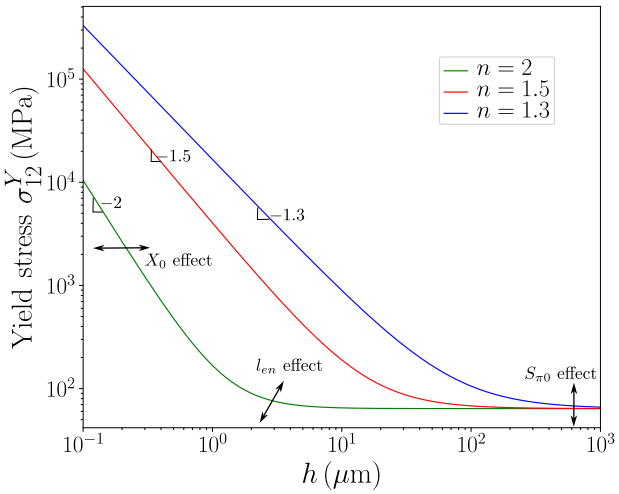

Fig. 10. Evolution of the yield stress σ^Y_{12} at 0.02% plastic strain as a function of the geometrical size h based on the analytical solution.

of the proposed models with only energetic effects (higher-order dissipative parts are neglected, $l_d = 0$) is considered for analytical analysis under monotonic shearing. Note that the two models are identical for this purely energetic problem. Since single- and double-slip configuration yield qualitatively similar result as shown by DDD, only the double-slip case ($\theta_1 = -\theta_2 = \theta = 60^\circ$) is analyzed. The slip systems satisfy:

$$\begin{cases} \mathbf{s}^\alpha = \cos\theta_\alpha\, \mathbf{e}_1 + \sin\theta_\alpha\, \mathbf{e}_2 \quad , \quad \mathbf{m}^\alpha = -\sin\theta_\alpha\, \mathbf{e}_1 + \cos\theta_\alpha\, \mathbf{e}_2 \\ \mathbf{s}^\alpha \cdot \mathbf{e}_3 = 0 \quad , \quad \mathbf{m}^\alpha \cdot \mathbf{e}_3 = 0 \quad , \quad \mathbf{l}^\alpha = \mathbf{s}^\alpha \times \mathbf{m}^\alpha = \mathbf{e}_3 \end{cases} \tag{53}$$

with the plastic slips γ^α independent of x_1 and x_3. In this case, the plastic slip gradients $\boldsymbol{\nabla}\gamma^\alpha$ lie in the plane $(\mathbf{e}_1, \mathbf{e}_2)$ and without losing any generality, the density of screw dislocations can be assumed to be considerably lower than that of edge dislocations, *i.e.,*:

$$\rho^\alpha_\odot = \mathbf{l}^\alpha \cdot \boldsymbol{\nabla}\gamma^\alpha = \mathbf{e}_3 \cdot \boldsymbol{\nabla}\gamma^\alpha = 0 \tag{54}$$

With the SGCP models, the top and bottom edges passivation is considered as:

$$\gamma^\alpha(x_1, -h/2, t) = \gamma^\alpha(x_1, h/2, t) = 0 \quad , \quad \text{for } \alpha = 1,\, 2 \quad \forall\, x_1, \quad \forall\, t \tag{55}$$

Analytical solution is derived hereafter for a general case ($X_0 \neq 0$, $l_{en} \neq 0$, $1 < n \leq 2$, $\cos 2\theta \neq 0$ and $\sin\theta \neq 0$). This solution will be compared with the FEM results. Under shear loading, only the component σ_{12} does not vanish and is constant through the strip. With the plastic strain incompressibility condition, the plastic slips on both slip systems are equal:

$$\gamma^1 = \gamma^2 = \gamma(x_2) \quad \Rightarrow \quad \varepsilon^p_{12}(x_2) = \gamma(x_2)\cos 2\theta \tag{56}$$

In the plastic regime and with the rate-independent formulation ($m \to 0$), the microscopic balance equation Eq. $(12)_1$ is expressed as:

$$\tau + X_0\, l_{en}^n |\sin\theta|^n \left(|\gamma_{,2}|^{n-2}\, \gamma_{,2}\right)_{,2} - \pi_0 = 0 \quad \text{with} \quad \tau = \sigma_{12}\cos 2\theta \quad \text{and} \quad \pi_0 = \text{sign}(\cos 2\theta) S_{\pi 0} \tag{57}$$

Integrating this differential equation leads to:

$$|\gamma_{,2}|^{n-2}\, \gamma_{,2} = -A_{n\theta}\, x_2 + B_1 \quad , \quad A_{n\theta} = \frac{\tau - \pi_0}{X_0\, l_{en}^n |\sin\theta|^n} \tag{58}$$

with B_1 an integration constant. Applying the boundary conditions in Eq. (55), the solution of the differential equation (58) is:

$$\gamma(x_2) = \frac{n-1}{n} A_{n\theta} |A_{n\theta}|^{\frac{2-n}{n-1}} \left[(h/2)^{\frac{n}{n-1}} - |x_2|^{\frac{n}{n-1}} \right] \quad , \quad A_{n\theta} = \frac{\tau - \pi_0}{X_0\, l_{en}^n |\sin\theta|^n} \tag{59}$$

Similar expressions with power-law defect energy have been derived by Bayerschen and Böhlke (2016) and Kuroda and Needleman (2023). Here, the orientation effect (anisotropy) of the systems is clearly shown through θ. The particular quadratic case $(n = 2)$ gives a parabolic plastic strain profile along the direction $\mathbf{e}_2$ and is well documented in the literature, (Bittencourt et al., 2003; Bittencourt, 2018). The mean plastic strain $\bar{\varepsilon}^p_{12}$ is deduced as:

$$\bar{\varepsilon}^p_{12} = \frac{\cos 2\theta}{h} \int_{-h/2}^{h/2} \gamma(x_2)\, \mathrm{d}x_2 = \cos 2\theta \frac{n-1}{(2n-1)} A_{n\theta} |A_{n\theta}|^{\frac{2-n}{n-1}} \left(\frac{h}{2}\right)^{\frac{n}{n-1}} \tag{60}$$

followed by the expression of the macroscopic stress:

$$\sigma_{12} = \frac{S_{\pi 0}}{|\cos 2\theta|} + X_0 \left(\frac{2n-1}{n-1}\right)^{n-1} \left|\frac{2\sin\theta}{\cos 2\theta}\right|^n \left(\frac{l_{en}}{h}\right)^n (\bar{\varepsilon}^p_{12})^{n-1} = \sigma_0 + H_{n\theta} (\bar{\varepsilon}^p_{12})^{n-1} \tag{61}$$

This result is analogous to a power-law hardening in the form of:

$$\sigma = K\left(\varepsilon^{p}\right)^{r} \tag{62}$$

with K and r material constants. Since X_0 is convoluted with l_{en} in the expression of the defect energy (Eqs. (33) and (50)), X_0 is fixed to be equal to the shear modulus μ in the rest of this work. Fig. 9 shows an example comparing the energetic theoretical results against the simulation for a non-quadratic case. The material parameters used are given in Tab. 2. The rate sensitivity parameters m and $\dot{\gamma}_0^{\alpha}$ are chosen adequately to approximate rate-independent results. The simulation and the analytical solution in Eq. (61) are in agreement, with a relative mean square error equals to 0.32% on the macroscopic response (the analytical solution is chosen as the reference), as demonstrated in Fig. 9a. Fig. 9b proves that, adopting $n < 2$ leads to a plastic strain with a plateau-like form around the center of the strip. This plateau region expands as l_{en} increases. Based on Eq. (61), it is possible to deduce the evolution of the yield stress σ_{12}^{Y} as function of h. Fig. 10 shows that the scaling exponent strictly equal to the power exponent n of the defect energy:

$$\sigma_{12}^{Y} \propto h^{-n} \tag{63}$$

It proves that considering only energetic SGCP is not enough to model size effects as experimentally observed (Petch, 1953; Mu et al., 2016; Zhang et al., 2023) or numerically seen with DDD as discussed in Section 2. Nonetheless, the analytical solution will be used to simplify the identification of some material parameters in the next section comparing the SGCP models with DDD. The role of higher-order dissipation in enriching the scaling relationship will be discussed in the next section.

5. Comparison of SGCP modeling capabilities with DDD

The ability of the proposed SGCP models to reproduce the DDD results is investigated in this section, considering the double-slip case. For this purpose, the influence of the major constitutive parameters (specially higher-order dissipative parameters) involved in the proposed SGCP models is studied prior to the comparison with DDD.

5.1. Prager-type model

Concerning the Prager-type model, the first- and higher-order hardening parameters denoted respectively by H_{π} and H_{ξ}, are fixed to zero, as the scope of this work focuses on the study of kinematic hardening effects. These two parameters only affect the isotropic hardening effects (Jebahi and Forest, 2023). The kinematic hardening effects are linked to the following parameters: higher-order Prager-type hardening modulus H_p, dissipative length scale l_d, initial first-order dissipative slip resistance $S_{\xi 0}$, energetic length scale l_{en} and defect energy exponent n. Their influence is investigated below. Subsequently, a direct discussion with DDD will be conducted.

5.1.1. Influence of parameters in the Prager-type model

The Prager-type model is first studied assuming $H_p = 0$ for a fixed geometrical size h. Based on Eq. $(36)_4$, this limit case corresponds to a vanishing Prager backstress $\mathbf{X}^{\alpha}$. It means that the higher-order dissipative part is only activated when the equivalent higher-order stress $\xi_{eq}^{\alpha} = \|\boldsymbol{\xi}^{\alpha}\| = S_{\xi 0} l_d$ in a rate-independent framework. Before this activation, the macroscopic response should be equal to the energetic solution. Fig. 11 shows the results of the case of $H_p = 0$ in comparison with the energetic analytical solution in terms of the macroscopic stress-strain response (Fig. 11a) and the plastic strain profile (Fig. 11b) for a non-quadratic case. Fig. 11a presents the expected behavior prior to saturation (activation of the higher-order yield function). Prior to saturation, an energetic response is obtained. The saturation stress can be

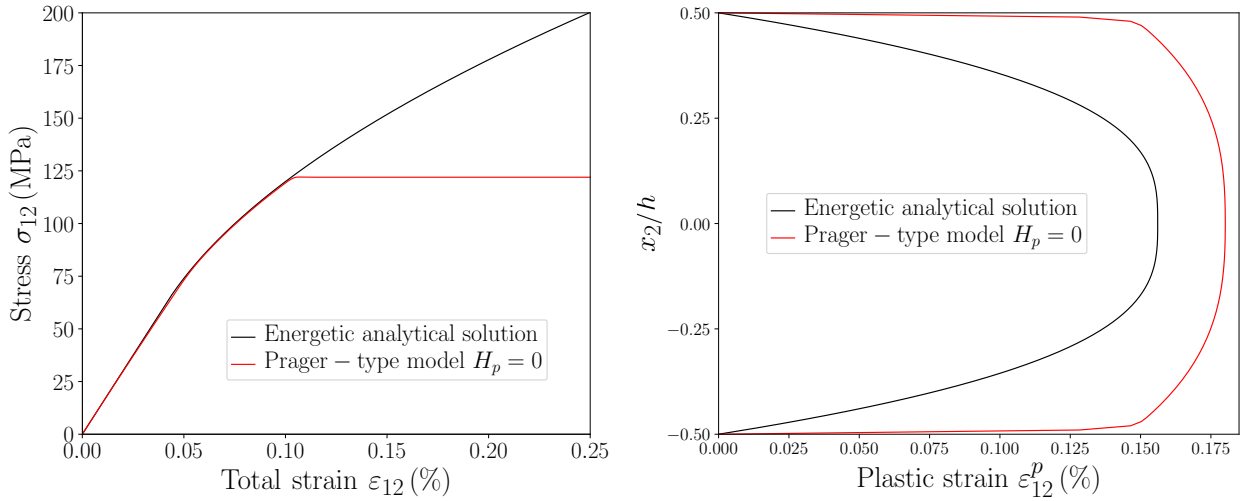

(a) Stress-strain curves.

(b) Plastic strain profile along $\mathbf{e}_2$ direction at $\varepsilon_{12} = 0.25\%$.

Fig. 11. Prager-type model: comparison with energetic analytical solution ($n = 1.5$, $l_d/h = 1$, $S_{\xi 0} = \tau_{\text{Peierls}}$).

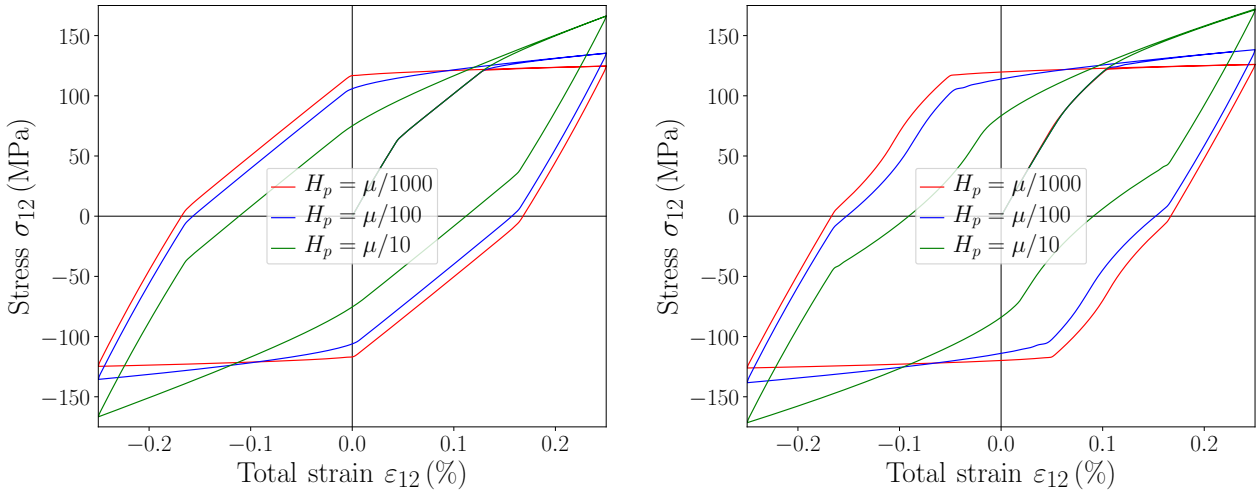

(a) Quadratic case ($n = 2$, $l_{en}/h = 1/4$).

(b) Non-quadratic case ($n = 1.5$, $l_{en}/h = 3/100$).

Fig. 12. Prager-type model: effect of the higher-order Prager modulus H_p ($l_d/h = 1$, $S_{\xi 0} = \tau_{\text{Peierls}}$).

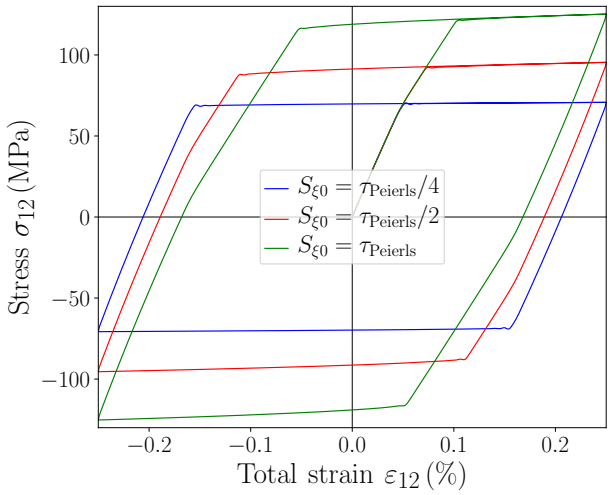

(a) Effect of $S_{\xi 0}$ ($l_{en}/h = 3/8$, $l_d/h = 1$).

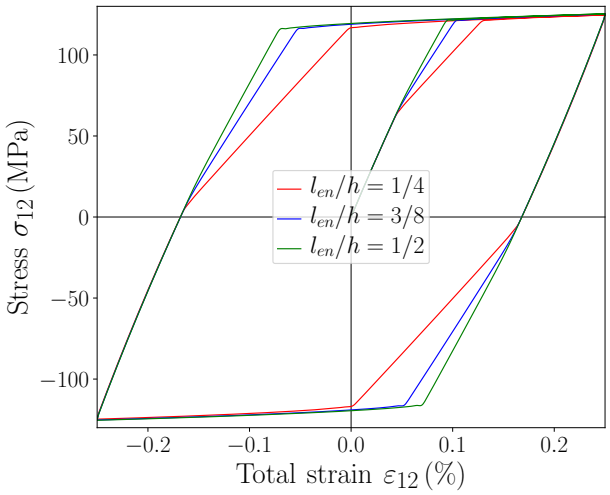

(b) Effect of l_{en} ($S_{\xi 0} = \tau_{\text{Peierls}}$, $l_d/h = 1$).

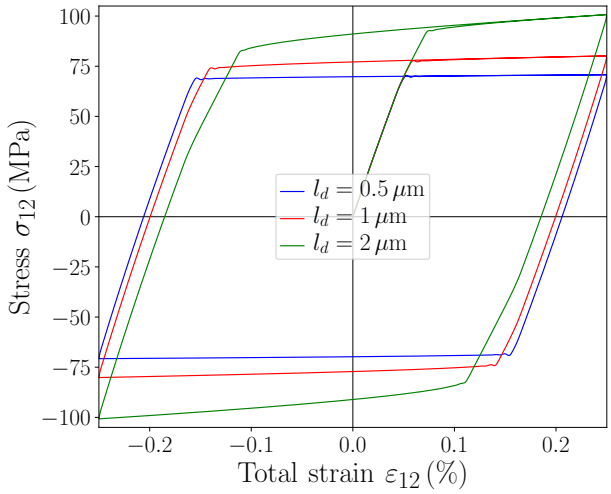

(c) Effect of l_d ($l_{en}/h = 3/8$, $S_{\xi 0} = \tau_{\text{Peierls}}/4$).

Fig. 13. Prager-type model: investigation of the effects of higher-order parameters $S_{\xi 0}$, l_{en}, l_d with fixed $n = 2$ and $H_p = \mu/1000$.

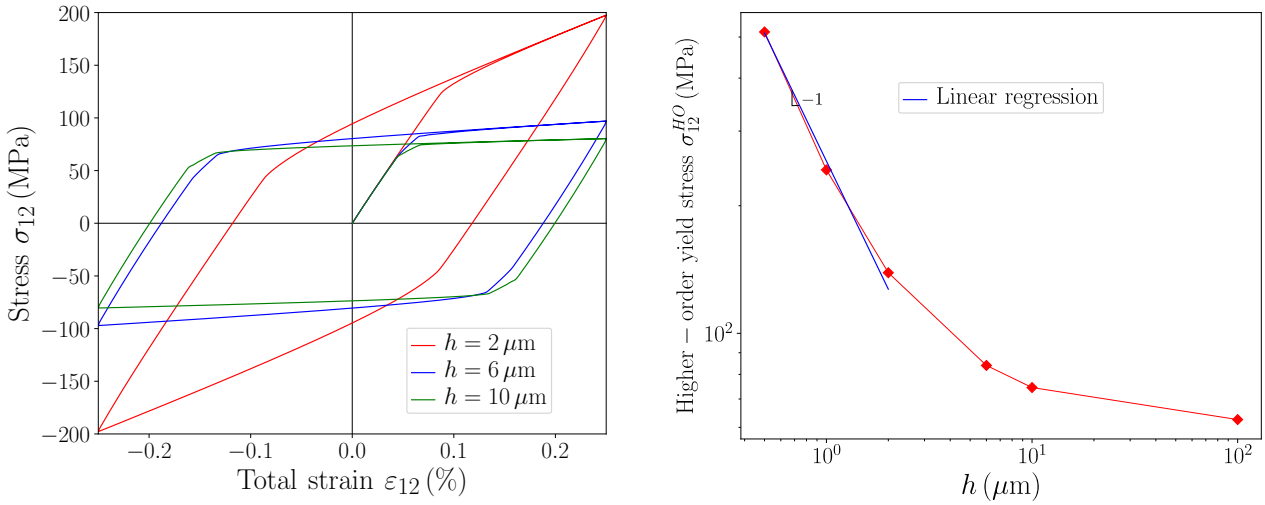

(a) Stress-strain curves.

(b) Log-log evolution of the apparent higher-order yield stress.

Fig. 14. Prager-type model: size effects in quadratic case ($l_{en} = 2\,\mu$m, $l_d = 1\,\mu$m, $H_p = \mu/10$, $S_{\xi 0} = \tau_{\text{Peierls}}$).

interpreted as apparent higher-order yield stress, beyond which the response saturates and becomes constant. It can be summarized that a two-stage plastic behavior is obtained. In terms of plastic strain profile, Fig. 11b exhibits once again a plateau-like form in the middle of the strip with a strong reduction of the thickness of the boundary layers, *i.e.,* small regions near the passivated edges characterized by rapid spatial evolution of the plastic shear strain, compared to the energetic case. Fig. 12 presents the effect of parameter H_p with an illustration in quadratic (Fig. 12a) and in non-quadratic (Fig. 12b) cases for the full cycle of shear loading. The two-stage plastic behavior is clearly visible, with H_p only influencing the post higher-order yielding. Increasing H_p leads to larger overall kinematic hardening.

For simplicity, effects of the parameters $S_{\xi 0}$, l_{en}, l_d are presented in Fig. 13 for the particular case of quadratic defect energy. Fig. 13a shows the influence of $S_{\xi 0}$ while keeping the other parameters fixed ($l_{en}/h = 3/8$, $l_d/h = 1$ and $H_p = \mu/1000$). An increase in $S_{\xi 0}$ results in a rise of the apparent higher-order yield stress. It results in a delay of the activation of the higher-order yield function. The hardening slopes before and after the higher-order yielding are not affected by $S_{\xi 0}$. This parameter only gives the level at which the steep-sloped micro-plasticity ends. On the other hand, changing l_{en}, gives a varying hardening slope of the micro-plasticity process as shown in Fig. 13b obtained with $S_{\xi 0} = \tau_{\text{Peierls}}$, $l_d/h = 1$ and $H_p = \mu/1000$. Increasing l_{en} yields narrower micro-plasticity zone although the same level of stress is needed before switching the slope. This can be linked to the effect of the total initial dislocation density in DDD simulations (Amouzou-Adoun et al., 2023). After the effects of $S_{\xi 0}$ and l_{en}, Fig. 13c presents the impact of l_d on the macroscopic stress-strain curves. Increasing l_d results first in a higher value of the apparent higher-order yield stress similarly to the effect of $S_{\xi 0}$. In a second time, the hardening slope after the activation of the higher-order yielding becomes greater with increasing l_d. This latter conclusion is comparable to the effect of the parameter H_p. The last-mentioned remark is in accordance with the definition of the higher-order Prager backstress as H_p is convoluted with l_d. To conclude, it would be possible without losing any generality to set l_d as a constant and determine the values of $S_{\xi 0}$ and H_p.

The role of n on the geometrical size effects is studied hereafter. Quadratic case ($n = 2$) is first analyzed in Fig. 14, while varying the geometrical size h with fixed $l_{en} = 2\,\mu$m, $l_d = 1\,\mu$m, $H_p = \mu/10$ and $S_{\xi 0} = \tau_{\text{Peierls}}$. The stress-strain curves in Fig. 14a show a strengthening phenomenon and an increasing of the kinematic hardening slope with decreasing size h. The smaller the size, the stronger the macroscopic response. One can argue that the strengthening is the result of the micro-plasticity process as described with

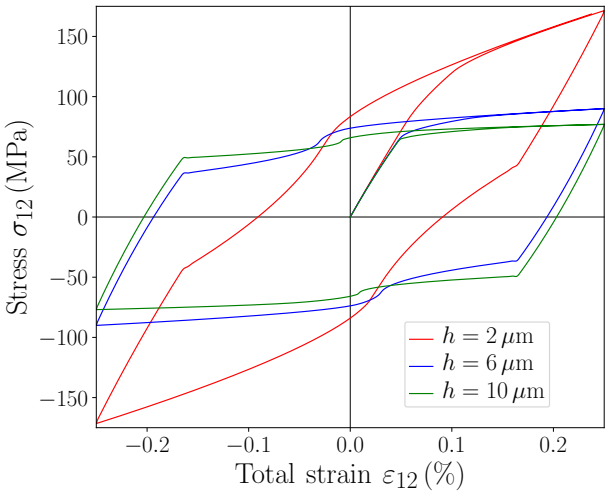

(a) Stress-strain curves.

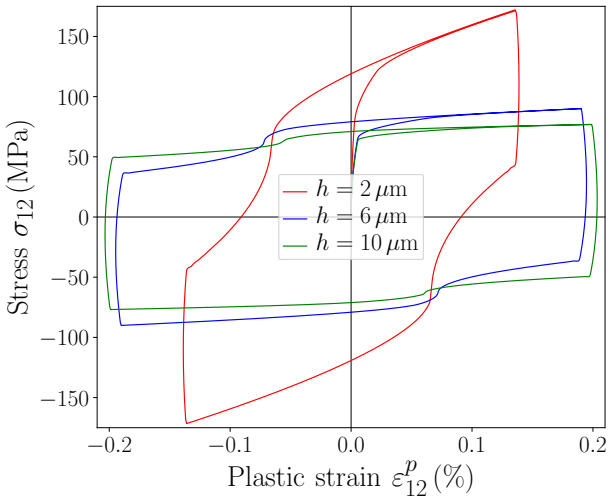

(b) Stress-Plastic strain curves.

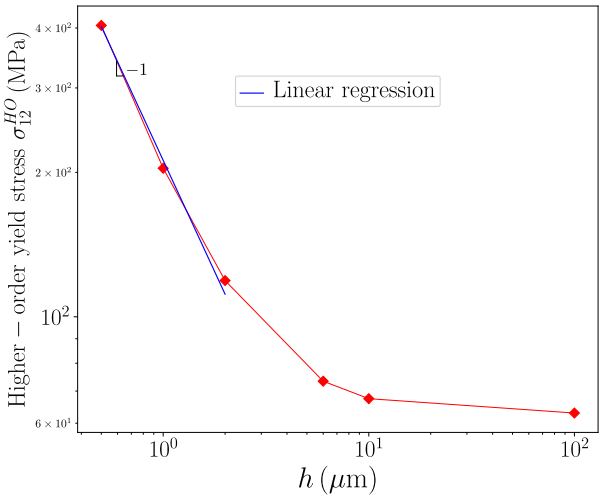

(c) Log-log evolution of the apparent higher-order yield stress.

Fig. 15. Prager-type model: size effects in non-quadratic case ($l_{en} = 0.06\,\mu$m, $l_d = 1\,\mu$m, $H_p = \mu/10$, $S_{\xi 0} = \tau_{\mathrm{Peierls}}$).

Tab. 3. Fitting material parameters for the Prager-type model based on DDD simulations.

Material parameter name	Symbol	Value	Unit
Initial first-order dissipative slip resistance	$S_{\pi 0}$	20	MPa
Initial higher-order dissipative slip resistance	$S_{\xi 0}$	40	MPa
Dissipative length scale	l_d	1	μm
Higher-order Prager modulus	H_p	$3\mu/20 = 11820$	MPa
Energetic length scale	l_{en}	0.18	μm
Exponent of the defect energy	n	1.6	$--$

the DDD results. This contrasts with the classical Gurtin-type SGCP models (Gurtin et al., 2007), where true "elastic-gaps" at the initial yield are observed. By extracting the apparent higher-order yield stress σ_{12}^{HO} as a function of the size h, a scaling relationship is deduced. Fig. 14b shows the log-log representation of σ_{12}^{HO} against h, showing a -1 scaling exponent. Fig. 15 presents the second analyzed non-quadratic case. Similar observations as in the quadratic case are obtained. Consequently, the following scaling relationship is deduced:

$$\sigma_{12}^{HO} \propto h^{-1} \quad , \quad \forall\, 1 \leq n \leq 2 \tag{64}$$

The introduction of the higher-order dissipation helps to improve the scaling relationship h^{-n} in Eq. (63) (obtained for a purely energetic problem) towards the classical Orowan law h^{-1}, which is still different from the obtained DDD scaling relationship $h^{-0.2}$ (see Eq. (3)). The defect energy exponent n can no more be interpreted as a scaling exponent. The advantage of using such less-than-quadratic defect energy is shown by the presence of the non-convex shape and a non-linear kinematic hardening (Fig. 15a and Fig. 15b). The difficulty with this Prager-type model lies in the fact that the inflection points are not centered around zero plastic strain. As evidenced by the DDD results and to the authors' best knowledge of experimental results, these inflection points are generally present around zero plastic strain. Indeed, this phenomenon corresponds to the "last to yield in forward loading is first to yield in reverse" process (Reynolds and Baxter, 2000).

5.1.2. Comparison with DDD

The influence of higher-order parameters on the plastic behavior has been investigated above. This subsection presents a direct comparison between the Prager-type model predictions and the DDD results. To this end, the model parameters are identified based on DDD results of the smaller grain size $h = 2\,\mu$m where marked size effects are observed. The analytical results are helpful in identifying some of these parameters Using the obtained parameters, the SGCP predictions for other grain sizes are compared with DDD results.

One needs to identify the six following material parameters: the initial first-order dissipative slip resistance $S_{\pi 0}$, the initial higher-order dissipative slip resistance $S_{\xi 0}$, the dissipative length scale l_d, the higher-order Prager modulus H_p, the energetic length scale l_{en} and the exponent of the defect energy n. $S_{\pi 0}$ describes the beginning of the micro-plasticity. By analyzing the DDD curves, $S_{\pi 0}$ is found to be in the same order of magnitude as the friction stress τ_{Peierls}. Here, the value $S_{\pi 0} = 20\,\text{MPa}$ is suitable. The hardening slope in the micro-plasticity is given by a combination of n and l_{en}. The smooth transition between the elasticity, the micro-plasticity and the well-established plasticity regime suggests that the value of n, in the range $1 \leq n \leq 2$, is not close to 2; otherwise, the transition would be sharp. Since this micro-plasticity for a given size h coincides with the analytical solution in Eq. (61), several iterations show that the combination of $n = 1.6$ and $l_{en} = 0.18\,\mu$m is a good compromise. Knowing that the apparent higher-order yield stress is influenced by l_d and $S_{\xi 0}$ and the kinematic hardening is given by the effect of l_d and H_p, it is sensible to fix l_d and to determine $S_{\xi 0}$ and H_p. For this reason, l_d is chosen to be $1\,\mu$m. $S_{\xi 0}$ is also in the same order of magnitude as τ_{Peierls}, and H_p can be linked to the shear modulus. The obtained parameters are summarized in Tab. 3. Fig. 16a shows the macroscopic curves of the SGCP fitting against the DDD results

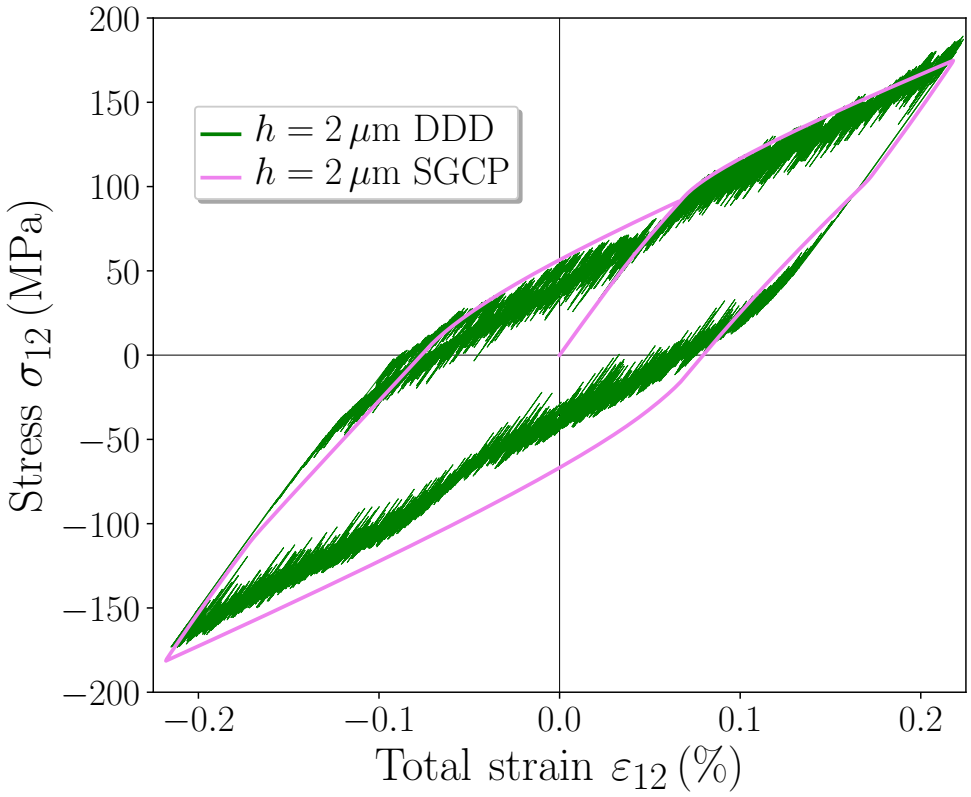

(a) Fitting on $h = 2\,\mu$m.

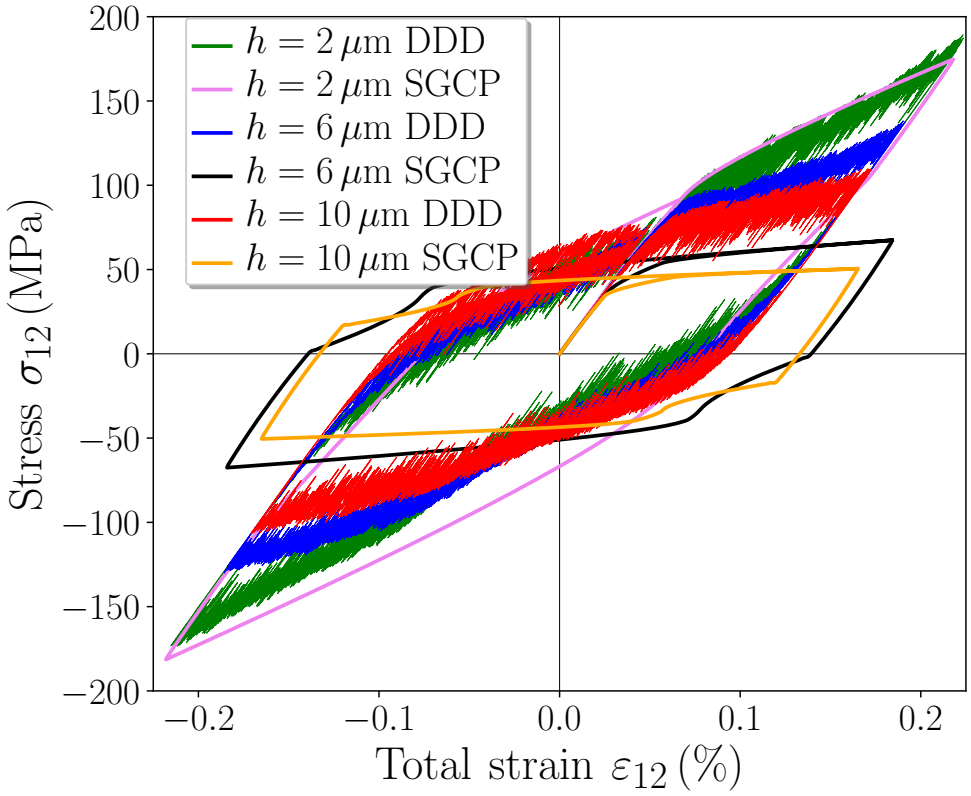

(b) DDD results versus SGCP (Prager-type) predictions.

Fig. 16. Prager-type model: identification and comparison of the proposed model with DDD results.

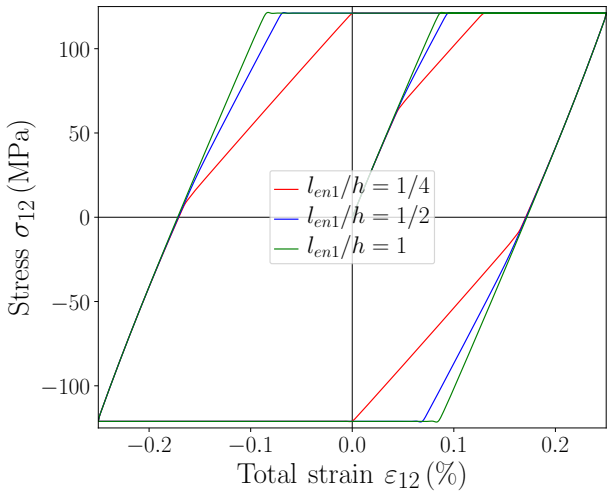

(a) Effect of l_{en1} with $l_{en2} = 0$.

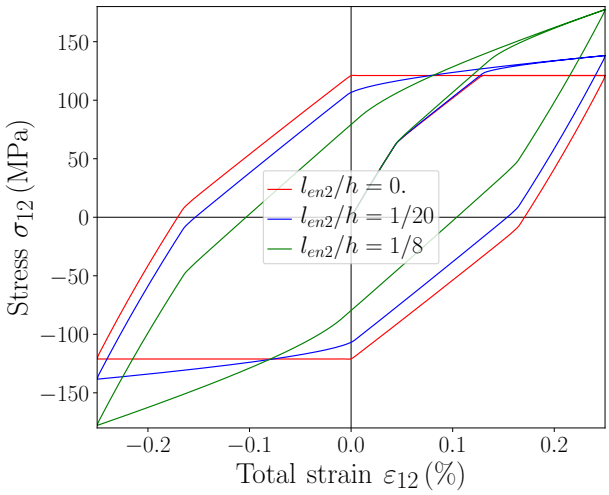

(b) Effect of l_{en2} with $l_{en1}/h = 1/4$.

Fig. 17. Multi-kinematic model: effect of the energetic length scales ($n_1 = n_2 = 2$, $l_d/h = 1$, $S_{\xi 1 0} = \tau_{\text{Peierls}}$).

for the particular size $h = 2\,\mu\text{m}$. A good fit is obtained in the loading part, but the response is not accurately reproduced in the reverse loading part. The non-convex shape happened just after the elastic unloading (*i.e.,* the plastic strain is still large). This is different from the DDD results. The predictions for the other grain sizes are presented in Fig. 16b. The macroscopic SGCP responses for $h = 6\,\mu\text{m}$ and $h = 10\,\mu\text{m}$ are lower than the DDD ones as a consequence of the scaling relationship h^{-1} in Eq. (64), obtained with the SGCP model. After the present investigation of the Prager-type model, the Chaboche-type (multi-kinematic) model will be studied in the next subsection, showing some improvements.

5.2. Chaboche-type (multi-kinematic) formulation

As a reminder, the multi-kinematic model has been implemented with two series decompositions, *i.e.,* $M = 2$. The first- and higher-order isotropic-like hardening parameters, respectively H_π and H_{ξ_i} are fixed to be zero for the same reasons as previously mentioned in the case of the Prager-type model. In this subsection, the role of following parameters are studied: dissipative length scale l_d, initial higher-order dissipative slip resistance $S_{\xi 1 0}$ (saturating value of $\boldsymbol{\xi}_1^\alpha$), energetic length scales l_{en1}, l_{en2} and defect energy exponents n_1 and n_2. It will be interesting to determine which defect energy exponent n_1 or n_2 should be taken less than quadratic. In consideration of the hypothesis of infinite $S_{\xi 2 0}$ (refer to Fig. 8), the effect of $S_{\xi 2 0}$ is not addressed. Comparison with DDD results will also be made.

5.2.1. Influence of parameters in the Chaboche-type model

The effect of the energetic length scales l_{en1} and l_{en2} are qualitatively insensitive to different values of the defect energy exponents n_1 and n_2. For this reason, Fig. 17 presents the outcomes of the study of the parameters l_{en1} and l_{en2} in terms of stress-strain curves with the double quadratic exponents $n_1 = n_2 = 2$, the dissipative length scale $l_d = h$ and initial higher-order dissipative slip resistance $S_{\xi 1 0} = \tau_{\text{Peierls}}$. Focusing on the loading part of the stress-strain curves, two plastic stages can be distinguished after the initial yielding, exactly like in DDD results. For this example, the values of l_{en1} and l_{en2} are chosen to emphasize this overall plastic behavior. It is clear from Fig. 17a that l_{en1} influences only the micro-plasticity response and has no effect on the well-established plasticity regime. This is explained by the fact that the l_{en1} is related to the higher-order stress $\boldsymbol{\xi}_1^\alpha$ which saturates. Employing a smaller value for l_{en1} leads to a less steep micro-plasticity phenomenon and a clear distinct manifestation of kinematic hardening. Conversely,

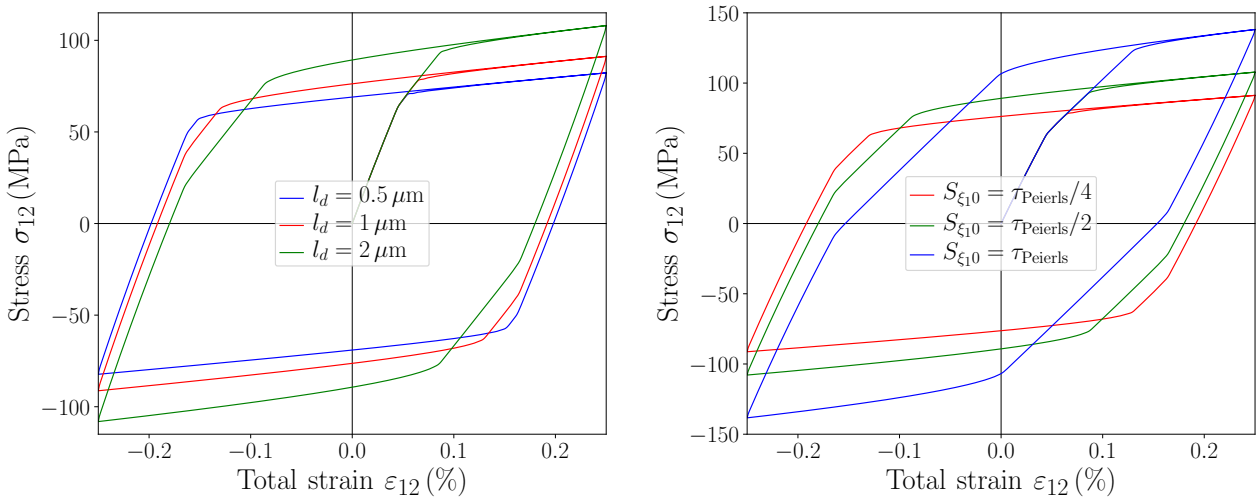

(a) Effect of l_d.

(b) Effect of $S_{\xi 0}$.

Fig. 18. Multi-kinematic model: investigation of the higher-order dissipative parameters ($h = 2\,\mu$m, $l_{en1}/h = 1/2$, $l_{en1}/l_{en2} = 5$).

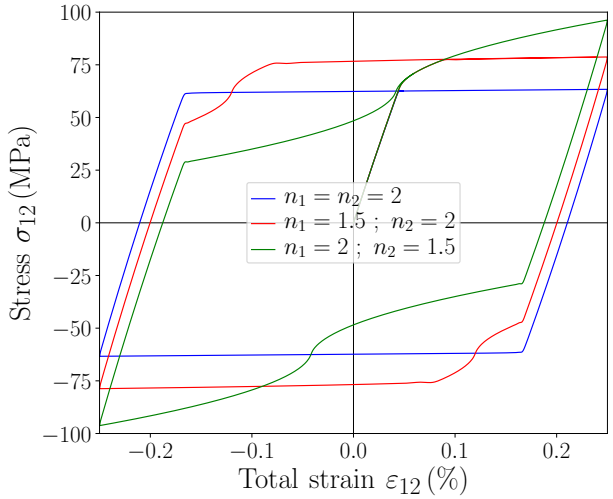

Fig. 19. Multi-kinematic model: investigation on the choice of the non-quadratic term in the defect energy ($h = 2\,\mu$m, $l_{en1} = l_{en2} = h/100$, $l_d = 1\,\mu$m, $S_{\xi 10} = \tau_{\text{Peierls}}/4$).

using a large value for l_{en1} yields a response that closely resembles the elastic one (quasi-elastic), with less noticeable kinematic hardening. Concerning l_{en2}, it influences both the micro-plasticity and the well-established plasticity regime as shown in Fig. 17b. Kinematic hardening is stronger for larger values of l_{en2}. It can be concluded that the micro-plasticity behavior is the combined result of l_{en1} and l_{en2} while the well-established plasticity regime remains unchanged with l_{en1}. As the hardening slope in the micro-plasticity regime is generally larger than the one in the well-established plasticity phase, l_{en1} will be chosen greater than or equal to l_{en2}.

Continuing with $n_1 = n_2 = 2$, the effects of the dissipative parameters l_d and $S_{\xi_1 0}$ are next studied. Fig. 18 provides a summary of the influence of the aforementioned parameters for a fixed geometrical size $h = 2\,\mu\text{m}$ and constant energetic length scales $l_{en1} = 0.5\,\mu\text{m}$ and $l_{en2} = 0.1\,\mu\text{m}$. The macroscopic stress-strain curves delineate the two-stage plastic behavior. Varying l_d, the apparent higher-order yield stress, at which the higher-order dissipation is activated, is affected as presented in Fig. 18a. Beyond the higher-order yielding, the hardening slope is unchanged with l_d. It is worth recalling that in the Prager-type model, this hardening slope is influenced by l_d. Fig. 18b illustrates the effect $S_{\xi_1 0}$. Changing the latter parameter, only the apparent higher-order yield stress varies. It can be inferred that both l_d and $S_{\xi_1 0}$ govern the same process. For the mentioned reason, l_d will be fixed to unity micron, *i.e.,* $l_d = 1\,\mu\text{m}$, in what follows to facilitate the identification of the model parameters. Here, l_d can be interpreted as a normalization dissipative parameter (Eq. (49)).

In the foregoing, the stress-strain curves are all of convex shape assuming double quadratic ($n_1 = n_2 = 2$) defect energy. However, when considering size effects, non-convex shapes may be observed, as discussed in Section 2 on DDD. In order to introduce this primordial aspect, it is necessary to choose which power exponent, n_1 or n_2, should be less than 2. For a given set of parameters $h = 2\,\mu\text{m}$, $l_{en1} = l_{en2} = h/100$, $l_d = 1\,\mu\text{m}$, $S_{\xi_1 0} = \tau_{\text{Peierls}}/4$, Fig. 19 presents a comparison of the double quadratic case with combination (quadratic and non-quadratic) cases. Choosing $n_1 = 1.5$ and $n_2 = 2$, *i.e.,* the only non-linear higher-order kinematic stresses are the saturating higher-order stresses $\boldsymbol{\xi}_1^\alpha$, a non-convex shape is obtained. The inflection points are close to the higher-order yield point under reserve loading. It is highly reminiscent of the result obtained with the Prager-type model. The KIII kinematic hardening of Asaro happens at large plastic strain contrary to the case of DDD where it is centered around zero plastic strain. Nevertheless, switching the non-linearity effect to the non-saturating higher-order kinematic stresses $\boldsymbol{\xi}_2^\alpha$, by choosing $n_1 = 2$ and $n_2 = 1.5$, leads to centered non-convexity in accordance with the DDD. Another advantage of this configuration is that the transition between the micro-plasticity and the post-activation of the higher-order yielding is quite smooth, which is consistent with DDD observations. For the rest of the present work, it will be kept that $\boldsymbol{\xi}_1^\alpha$ is always linear while $\boldsymbol{\xi}_2^\alpha$ is non-linear with an exponent $n_2 < 2$, which needs to be determined.

Prior to the identification with DDD results, it is interesting to investigate the scaling relationship obtained with the multi-kinematic approach including higher-order dissipation. Fig. 20 presents the log-log evolution of the apparent higher-order yield stress as a function of the geometrical size h for a given set of parameters. Similarity with the purely energetic formulation shown in Fig. 10 and the Prager-type formulation shown in Figs. 14b and 15c is apparent in terms of a linear evolution for small size h and an asymptotic one for very large size h. Regardless of the value of n_2, a saturating scaling exponent of -1 is obtained:

$$\sigma_{12}^{HO} \propto h^{-1} \quad , \quad \forall n_2 \quad \text{with} \quad n_1 = 2 \tag{65}$$

As obtained with the Prager-type formulation (see Eq. (64)), this scaling relationship is an improvement compared with the energetic solution in Eq. (63) and is in agreement with the established Orowan relation for precipitate and inclusion size effects. Further refinements in this gradient-enhanced theory are still needed to get to the scaling relationship found in Eq. (3) with a scaling exponent of -0.2. Meanwhile, the hardening after the activation of the higher-order yield functions, evolves as h^{-n_2} based on Eq. (61) since the post higher-order yielding response is only given by $\boldsymbol{\xi}_2^\alpha$. It is worth recalling that the hardening in this regime evolves as $h^{-0.5}$ in DDD results. The multi-kinematic model has demonstrated significant flexibility

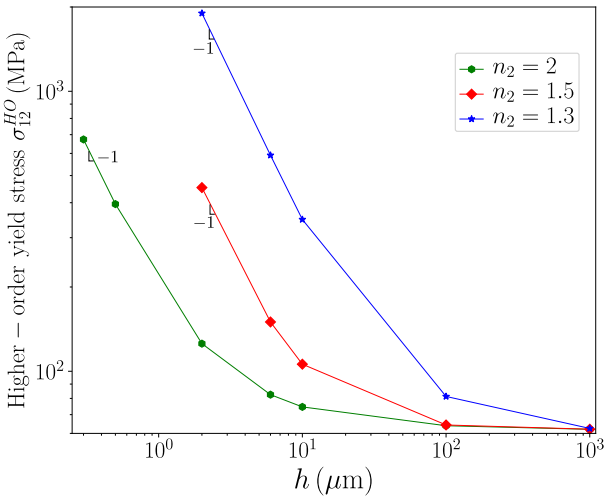

Fig. 20. Multi-kinematic model: evolution of apparent higher-order yield stress σ_{12}^{HO} as function of the size h based on the proposed multi-kinematic model ($l_{en1} = 0.5\,\mu$m, $l_{en2} = 0.25\,\mu$m, $l_d = 1\,\mu$m, $n_1 = 2.$).

Tab. 4. Fitting material parameters for the multi-kinematic model based on DDD simulations.

Material parameter name	Symbol	Value	Unit
Initial first-order dissipative slip resistance	$S_{\pi 0}$	20	MPa
First (decomposition) initial higher-order dissipative slip resistance	$S_{\xi_1 0}$	20	MPa
Dissipative length scale	l_d	1	μm
First energetic length scale	l_{en1}	1.5	μm
Second energetic length scale	l_{en2}	0.09	μm
First exponent of the defect energy	n_1	2	$--$
Second exponent of the defect energy	n_2	1.6	$--$

in replicating the observed plastic behavior with DDD. This point is further investigated in the following subsection providing a direct comparison with DDD outcomes for shear and tension-compression loading.

5.2.2. Comparison with DDD for shearing

In the same way as with the Prager-type model, the parameter related to the Chaboche-type formulation are identified on the DDD results of the geometrical size $h = 2\,\mu$m (see green curves in Fig. 3).

It was previously demonstrated that the first exponent defect energy, n_1, is set to be equal to 2, and the dissipative length scale, l_d, to $1\,\mu$m. In this case, five material parameters have to be identified: the initial first-order dissipative slip resistance $S_{\pi 0}$, the first initial higher-order dissipative slip resistance $S_{\xi_1 0}$, the energetic length scales l_{en1} and l_{en2}, and the second exponent of the defect energy n_2. It is appropriate to start by fitting the second exponent n_2 and the second energetic length scale l_{en2}, knowing that the hardening in the well-established plasticity regime depends only on $\boldsymbol{\xi}_2^{\alpha}$. In this case, the value of n_2 can be calculated using power-law hardening in Eq. (62) so that $n_2 = r + 1$. This suggests that $n_2 = 1.6$ is a suitable fitting value. The second energetic length scale l_{en2} can then be calibrated using the analytical solution in Eq. (61) in order to reproduce the DDD hardening for $h = 2\,\mu$m. Next, $S_{\pi 0}$, $S_{\xi_1 0}$, l_{en1} are determined to reproduce the initial yielding and the micro-plasticity response. These calibrated parameters are summarized in Tab. 4. Note that $S_{\pi 0}$, $S_{\xi_1 0}$ are both found to be close to τ_{Peierls}. The derived length scales, $l_{en1} = 1.5\,\mu$m and $l_{en2} = 0.09\,\mu$m, are of the same order of magnitude as the inverse of the square root of the initial dislocation density $1/\sqrt{\rho_0^{DDD}} = 0.577\,\mu$m, which can be viewed as a characteristic length scale (Dahlberg and Boåsen, 2019).

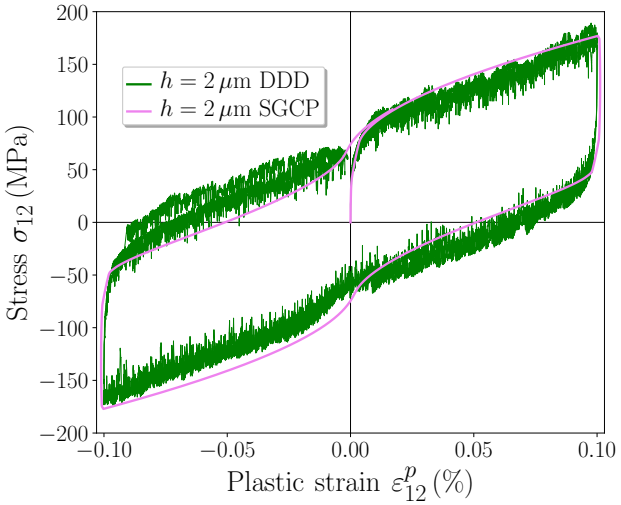

(a) Fitting on $h = 2\,\mu$m: σ_{12} versus ε^p_{12}.

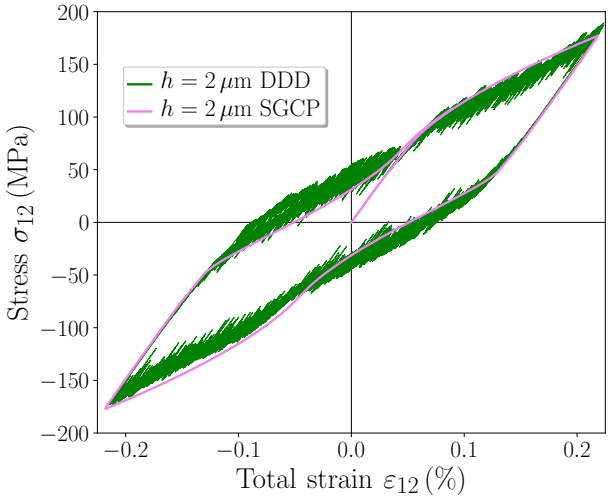

(b) Fitting on $h = 2\,\mu$m: σ_{12} versus ε_{12}.

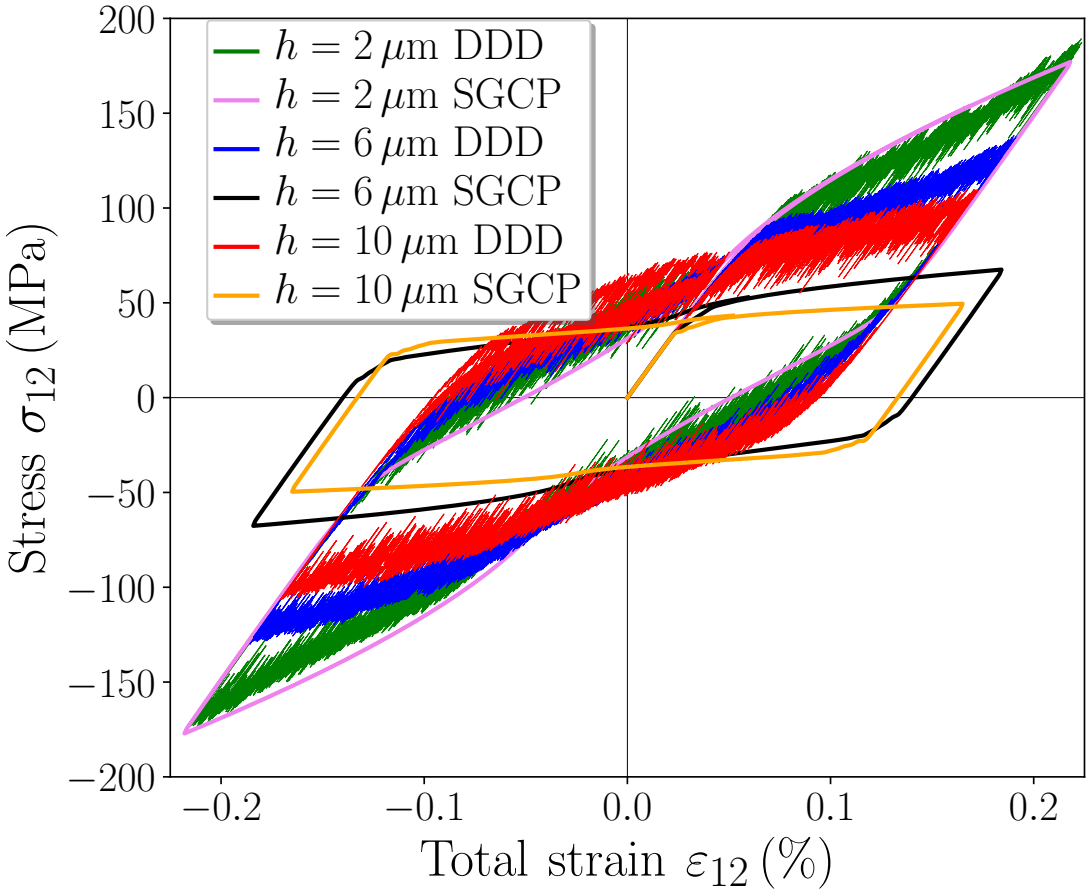

(c) DDD results versus SGCP (multi-kinematic) predictions.

Fig. 21. Multi-kinematic model: identification and comparison of the proposed model with DDD results.

Fig. 21 presents the obtained macroscopic stress-strain response for the geometrical size $h = 2\,\mu\mathrm{m}$, which was used for the identification process, as well as the predictions for the other geometrical sizes $h = 6\,\mu\mathrm{m}$ and $h = 10\,\mu\mathrm{m}$, utilizing the identified parameters. According to Fig. 21a where the macroscopic stress is plotted as a function of the plastic strain for the case $h = 2\,\mu\mathrm{m}$, the multi-kinematic model demonstrates a high degree of fidelity in regard with DDD, as it successfully replicates micro-plasticity, plastic hardening, and KIII kinematic hardening of Asaro. The corresponding stress-strain is shown in Fig. 21b. This means that the proposed model can accurately reproduce all the DDD observed features. Finally, Fig. 21c presents the results for all the grain sizes. For $h = 6\,\mu\mathrm{m}$ and $h = 10\,\mu\mathrm{m}$, the model predicts that the KIII kinematic hardening of Asaro becomes less marked as expected. This last remark falls perfectly in the scope of the DDD results. The non-convex shape is clearly a manifestation of size effects. Nevertheless, the scaling exponent of -1 obtained with the multi-kinematic model, in comparison with the -0.2 with DDD, indicates that there is a quantitative difference between the predicted curves with the continuum model and DDD. As illustrated in Fig. 21c, the predicted responses for $h = 6\,\mu\mathrm{m}$ and $h = 10\,\mu\mathrm{m}$ are found to be underestimated with this continuum model in reference to the DDD responses.

5.2.3. Prediction of the tension-compression

Using the previously identified parameters in the shearing case (see Tab. 4), tension-compression simulations are conducted and compared with the DDD results in the configuration shown in Fig. 1c. Fig. 22 presents the detail macroscopic responses. The general conclusions on the plastic activity are still valid. The two-stage plastic behavior and the type III (KIII) kinematic hardening of Asaro are still observed. However, it is evident that the model overestimates the strengthening and hardening in the well-established plasticity regime when using the obtained parameters from shearing. The transfer of parameters from one loading to a different one is not trivial. The dislocation structures undergo significant alterations in response to the loading type, resulting in notable changes in the internal stresses which has to be better considered by the continuum models.

6. Conclusion

Shearing and tension-compression tests have been studied with DDD for single- and double-slip cases. The simulations show strengthening and dominating kinematic hardening effects. An accent was put on the strengthening phenomenon, *i.e.,* the increase of the yield stress with geometrical size h. The apparent higher-order yield stress results from a micro-plasticity process which is characterized by a high hardening slope, at very low plastic level. This explanation echoes experimental works (Fleck et al., 1994; Hua et al., 2021; Xie et al., 2023). The apparent higher-order yield stress is found to evolve as $h^{-0.2}$ for the shearing case and as $h^{-0.3}$ for the tension-compression case. The scaling exponent depends then on the nature of the loading and the initial dislocation configuration. These findings are similar to the experimental conclusions in (Dunstan and Bushby, 2014; Mu et al., 2016). Beyond this apparent higher-order yield stress, a well-established plasticity regime takes place and is also size-dependent. The hardening slope in this plastic activity is found to evolve as $h^{-0.5}$ for the shearing case and $h^{-1.1}$ for the tension-compression case. The analysis of the full cyclic loading reveals a dominating kinematic hardening with respect to isotropic hardening. The presence of inflection points around zero plastic strain on the macroscopic curves under reverse loading, is also observed. This uncommon non-convex shape of on the macroscopic curves is identified by the type III (KIII) kinematic hardening of Asaro (Asaro, 1975; Stoltz and Pelloux, 1976; Proudhon et al., 2008), which is considered to be the closest to a perfect plastic recovery process. This non-convex shape becomes less marked for large grains and more classical Bauschinger effects are observed.

Based on the conclusions of DDD simulations, two SGCP models of higher-order kinematic hardening modeling are proposed. Using the framework of kinematic decomposition of the plastic slip gradient into

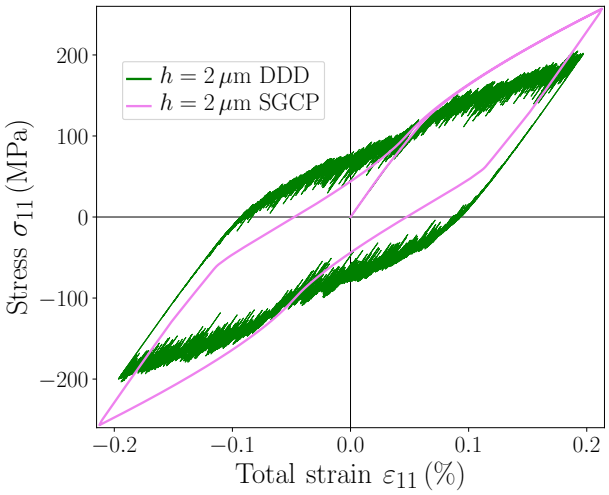

(a) $h = 2\,\mu$m: σ_{11} versus ε_{11}.

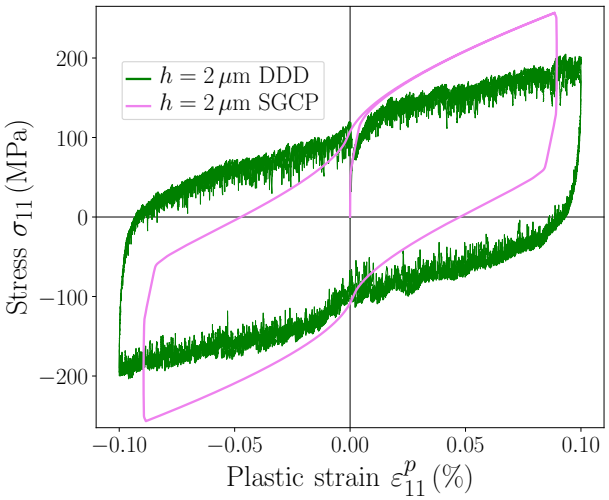

(b) $h = 2\,\mu$m: σ_{11} versus ε^p_{11}.

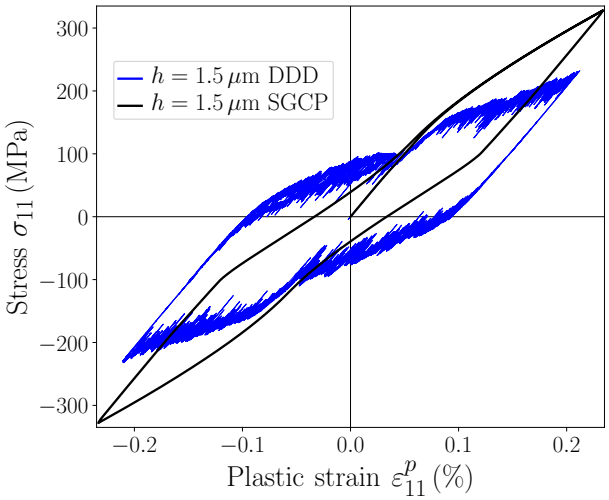

(c) $h = 1.5\,\mu$m.

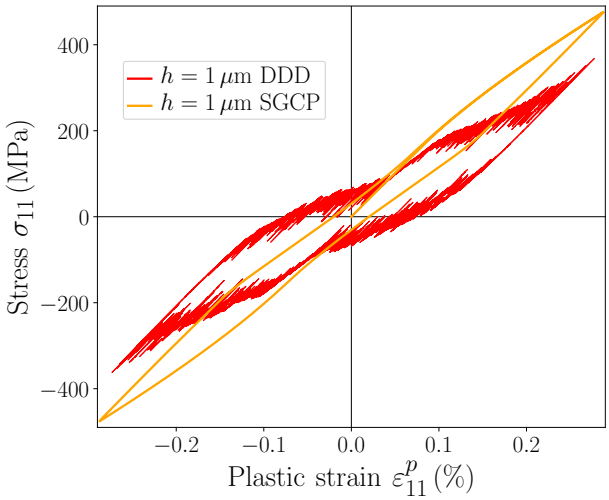

(d) $h = 1\,\mu$m.

Fig. 22. Predictions in tension-compression of the multi-kinematic model versus the DDD results with the identified parameters.

recoverable (energetic) and unrecoverable (dissipative) parts, the defect energy is enriched to account for supplementary higher-order kinematic hardening. The first proposed model is based on a Prager-type approach with the introduction of a backstress related to the dissipative part of the plastic slip gradient. Strengthening caused by a micro-plasticity process is observed as with DDD. The obtained apparent higher-order yield stress evolves as h^{-1} (Orowan scaling law). The model also integrates a less-than-quadratic defect energy with an exponent n, which helps to reproduce in a natural way the KIII kinematic hardening of Asaro. However, with this Prager-type approach, the inflection points are generally visible for positive plastic strain. This particular aspect is improved with the second proposed model based on the multi-kinematic decomposition of the plastic slip gradients. This approach echoes Chaboche modeling technique of the kinematic hardening, where the work-conjugate higher-order stress is given by a superimposition of several independent kinematic variables. Here, the defect energy is a combination of quadratic and non-quadratic terms. The quadratic term is associated with a saturating higher-order stress and the non-quadratic term with a non-saturating higher-order stress. This concept helps to reproduce the non-convex shape around zero plastic strain, particularly as in DDD results. Nonetheless, the apparent higher-order yield stress with the multi-kinematic model also evolves as h^{-1}. This seems to be a notable limitation of SGCP theories. To date, no SGCP theory predicts a scaling exponent less than -1. An attempt of calibration with DDD results for a selected size h is done and it has confirmed that the Chaboche-type model is more in accordance with DDD than the Prager-type model.

In order to improve the scaling relationship, the proposed kinematic decomposition approaches can be used in the micromorphic formulation of the "curl $\mathbf{H}_p$" model (Cordero et al., 2010). This is an on-going investigation and will be treated in a future work. This type of model is less expensive since the number of degrees of freedom is reduced. It is then recommended to compare and calibrate the model with 3D experiments (Mu et al., 2016; Zhang et al., 2023). Extension to poly-crystal cases (Cordero et al., 2013) should also be possible by integrating realistic interface conditions and including evolving internal length scales (Hunter and Koslowski, 2008; Dahlberg and Boåsen, 2019) within strain gradient-enhanced framework. Another improvement could be made by using the gradient of saturating plastic variables (Abatour and Forest, 2023).

Acknowledgments

The authors acknowledge the financial support of the French National Research Agency (ANR) under reference ANR-20-CE08-0010 (SGP-GAPS project https://www.sgpgaps.fr/).

Appendix A. Finite element numerical implementation

The numerical finite element (FEM) implementation in ABAQUS/Standard of the proposed models is described in this section.

Considering Dirichlet (essential) boundary conditions applied on portions of the studied domain boundary, let $\delta\dot{\mathbf{u}}$ and $\delta\dot{\boldsymbol{\gamma}}$ be test fields kinematically admissible to $\mathbf{0}$ on these portions. The weak forms of the macroscopic and microscopic balance equations, *i.e.*, $(11)_1$ and $(12)_1$, can be expressed as:

$$\begin{aligned} G_u &= \int_{\mathcal{V}} \delta\dot{\boldsymbol{\varepsilon}} : \boldsymbol{\sigma}\, dv - \int_{\mathcal{S}_t} \delta\dot{\mathbf{u}} \cdot \mathbf{t}\, ds \\ G_\gamma &= \sum_{\alpha=1}^{q} \int_{\mathcal{V}} \boldsymbol{\nabla}\delta\dot{\gamma}^\alpha \cdot \boldsymbol{\xi}^\alpha\, dv + \sum_{\alpha=1}^{q} \int_{\mathcal{V}} \delta\dot{\gamma}^\alpha\, \pi^\alpha\, dv - \sum_{\alpha=1}^{q} \int_{\mathcal{V}} \delta\dot{\gamma}^\alpha\, \tau^\alpha\, dv - \sum_{\alpha=1}^{q} \int_{\mathcal{S}_\chi^\alpha} \delta\dot{\gamma}^\alpha\, \chi^\alpha\, ds \end{aligned} \tag{A.1}$$

where $\mathcal{S}_t$ and $\mathcal{S}_\chi^\alpha$ are respectively the portions of the studied domain boundary on which macroscopic and microscopic traction, respectively denoted by $\mathbf{t}$ and χ^α, are enforced. The finite element method is employed to solve numerically these weak forms. For this purpose, a User-ELement (UEL) subroutine is implemented in the commercial software ABAQUS/Standard, with the degrees of freedom being the displacement and

plastic slip fields ($\mathbf{u}$ and γ^α). In 2D case, giving a finite element with 2×2 Gauss integration points, quadratic (eight-noded) $\mathbf{u}$-interpolation and linear (four-noded) γ^α-interpolation are adopted. In this element, the displacement and plastic slip fields are estimated as:

$$u_i\left(x_1,x_2\right)=\sum_{k=1}^{8}N_k^u\left(x_1,x_2\right)\,U_i^k,\quad \gamma^\alpha\left(x_1,x_2\right)=\sum_{k=1}^{4}N_k^\gamma\left(x_1,x_2\right)\,\Gamma_k^\alpha \tag{A.2}$$

where U_i^k and Γ_k^α are respectively the nodal values of the displacement component u_i and the plastic slip γ^α, and N_k^u and N_k^γ are the associated interpolation (shape) functions. With these interpolated fields, the previously mentioned weak forms in Eq. (A.1) are written, in matrix form, within a representative finite element as follows:

$$\begin{aligned}
G_u^e &= \left(\delta\dot{\underline{U}}^e\right)^T\cdot\left(\int_{\mathcal{V}^e}\underline{\underline{B}}_u^T\cdot\underline{\sigma}\,dv-\int_{\mathcal{S}_t^e}\underline{\underline{N}}_u^T\cdot\underline{t}\,ds\right)\\
G_\gamma^e &= \left(\delta\dot{\underline{\Gamma}}^e\right)^T\cdot\left(\int_{\mathcal{V}^e}\underline{\underline{B}}_\gamma^T\cdot\underline{\xi}\,dv+\int_{\mathcal{V}^e}\underline{\underline{N}}_\gamma^T\cdot\underline{\pi}\,dv-\int_{\mathcal{V}^e}\underline{\underline{N}}_\gamma^T\cdot\underline{\tau}\,dv-\int_{\mathcal{S}_\chi^e}\underline{\underline{N}}_\gamma^T\cdot\underline{\chi}\,ds\right)
\end{aligned} \tag{A.3}$$

where $\underline{\sigma}$, $\underline{\pi}$ and $\underline{\xi}$ are vector representations of the macroscopic and microscopic stresses combining those defined on all slip systems, $\underline{\tau}$ is a vector containing the resolved shear stresses on all slip systems, $\underline{t}$ is the macroscopic traction vector, $\underline{\chi}$ is a vector containing the microscopic traction scalars associated with all the slip systems, $\underline{\underline{N}}_u$ and $\underline{\underline{B}}_u$ are interpolation and gradient matrices associated with the displacement field, and $\underline{\underline{N}}_\gamma$ and $\underline{\underline{B}}_\gamma$ are interpolation and gradient matrices associated with the plastic slip fields. The principle of virtual power implies that G_u^e and G_γ^e are zero for any virtual variations of the element nodal variables $\delta\dot{\underline{U}}^e$ and $\delta\dot{\underline{\Gamma}}^e$. It leads to the following residuals:

$$\begin{aligned}
\underline{R}_u^e &= \int_{\mathcal{V}^e}\underline{\underline{B}}_u^T\cdot\underline{\sigma}\,dv-\int_{\mathcal{S}_t^e}\underline{\underline{N}}_u^T\cdot\underline{t}\,ds &&= \underline{0}\\
\underline{R}_\gamma^e &= \int_{\mathcal{V}^e}\underline{\underline{B}}_\gamma^T\cdot\underline{\xi}\,dv+\int_{\mathcal{V}^e}\underline{\underline{N}}_\gamma^T\cdot\underline{\pi}\,dv-\int_{\mathcal{V}^e}\underline{\underline{N}}_\gamma^T\cdot\underline{\tau}\,dv-\int_{\mathcal{S}_\chi^e}\underline{\underline{N}}_\gamma^T\cdot\underline{\chi}\,ds &&= \underline{0}
\end{aligned} \tag{A.4}$$

These equations are linearized with respect to the variations of the element nodal variables $\underline{U}^e$ and $\underline{\Gamma}^e$, which results in an elementary system of equations that can be presented in matrix form as:

$$\begin{bmatrix}\underline{\underline{K}}_{uu}^e & \underline{\underline{K}}_{u\gamma}^e\\ \underline{\underline{K}}_{\gamma u}^e & \underline{\underline{K}}_{\gamma\gamma}^e\end{bmatrix}\begin{bmatrix}\Delta\underline{U}^e\\ \Delta\underline{\Gamma}^e\end{bmatrix}=\begin{bmatrix}-\underline{R}_u^e\\ -\underline{R}_\gamma^e\end{bmatrix} \tag{A.5}$$

with:

$$\underline{\underline{K}}_{uu}^e=\frac{\partial\underline{R}_u^e}{\partial\underline{U}^e},\quad \underline{\underline{K}}_{u\gamma}^e=\frac{\partial\underline{R}_u^e}{\partial\underline{\Gamma}^e},\quad \underline{\underline{K}}_{\gamma u}^e=\frac{\partial\underline{R}_\gamma^e}{\partial\underline{U}^e},\quad \underline{\underline{K}}_{\gamma\gamma}^e=\frac{\partial\underline{R}_\gamma^e}{\partial\underline{\Gamma}^e} \tag{A.6}$$

After assembling, the obtained global non-linear system of equations is solved using Newton-Raphson iterative scheme.

Appendix B. Integration algorithm of the constitutive laws associated with the Prager-type model

The state laws in Eq. (37) are integrated with the Alg. 1, see next page.

Algorithm 1 Integration of the constitutive equations at the integration points of the Prager-type model

Inputs: $\boldsymbol{\varepsilon}_e$, $\boldsymbol{\varepsilon}_p$, $\boldsymbol{\kappa}_r^\alpha$, $\boldsymbol{\kappa}_d^\alpha$, $\Delta\mathbf{u}$, $\Delta\gamma^\alpha$, S_π^α, S_ξ^α, $\boldsymbol{\sigma}$, π^α, $\boldsymbol{\xi}^\alpha$, $\mathbf{X}^\alpha$

Compute: $\Delta\boldsymbol{\varepsilon} = [\nabla(\Delta\mathbf{u})]_{sym}$, $\Delta\boldsymbol{\varepsilon}_p = \sum_{\alpha=1}^{q} \Delta\gamma^\alpha \, \mathbf{P}^\alpha$, $\Delta\boldsymbol{\varepsilon}_e = \Delta\boldsymbol{\varepsilon} - \Delta\boldsymbol{\varepsilon}_p$

Compute: $\boldsymbol{\varepsilon}_e = \boldsymbol{\varepsilon}_e + \Delta\boldsymbol{\varepsilon}_e$, $\boldsymbol{\varepsilon}_p = \boldsymbol{\varepsilon}_p + \Delta\boldsymbol{\varepsilon}_p$

Compute: $\boldsymbol{\sigma} = \lambda \, \mathrm{tr}(\boldsymbol{\varepsilon}_e) \, \mathbf{I} + 2\,\mu\,\boldsymbol{\varepsilon}_e$

Do $\alpha = 1$ **to** q**:**

  Compute: $\Delta e_\pi^\alpha = |\Delta\gamma^\alpha|$

End do

Do $\alpha = 1$ **to** q**:**

  Compute: $\Delta S_\pi^\alpha = \sum_{\beta}^{q} H_\pi \, \Delta e_\pi^\beta$

  Compute: $S_\pi^\alpha = S_\pi^\alpha + \Delta S_\pi^\alpha$

  Compute: $\pi^\alpha = S_\pi^\alpha \left[\frac{\Delta e_\pi^\alpha}{\Delta t\,\dot{\gamma}_0^\alpha}\right]^m \frac{\Delta\gamma^\alpha}{\Delta e_\pi^\alpha}$

End do

Initialization:

  Do $\alpha = 1$ **to** q**:**

    Compute: $\Delta\boldsymbol{\kappa}^\alpha = \nabla(\Delta\boldsymbol{\gamma}^\alpha)$, $\Delta\boldsymbol{\kappa}_r^\alpha = \Delta\boldsymbol{\kappa}^\alpha$, $\boldsymbol{\kappa}_r^\alpha = \boldsymbol{\kappa}^\alpha + \Delta\boldsymbol{\kappa}_r^\alpha$, $\Delta\boldsymbol{\kappa}_d^\alpha = \mathbf{0}$, $\Delta\kappa_d^\alpha = 0$

    Compute: $\mathbf{A}^{\alpha\alpha} = (n-1)\; X_0\, l_{en}^n \left[|\mathbf{s}^\alpha \cdot \boldsymbol{\kappa}_r^\alpha|^{n-2}\; \mathbf{s}^\alpha \otimes \mathbf{s}^\alpha + |\mathbf{l}^\alpha \cdot \boldsymbol{\kappa}_r^\alpha|^{n-2}\; \mathbf{l}^\alpha \otimes \mathbf{l}^\alpha\right]$

    Compute: $\Delta\boldsymbol{\xi}^\alpha = \mathbf{A}^{\alpha\alpha} \cdot \Delta\boldsymbol{\kappa}_r^\alpha$, $\boldsymbol{\xi}^\alpha = \boldsymbol{\xi}^\alpha + \Delta\boldsymbol{\xi}^\alpha$

    Compute: $\Delta\mathbf{X}^\alpha = H_p\, l_d^2\, \Delta\boldsymbol{\kappa}_d^\alpha$, $\mathbf{X}^\alpha = \mathbf{X}^\alpha + \Delta\mathbf{X}^\alpha$

    Compute: $F^\alpha = \|\boldsymbol{\xi}^\alpha - \mathbf{X}^\alpha\|$

  End do

  $\mathbf{F} = \left[F^1, \ldots, F^q\right]^T$

End initialization

While ($\|\mathbf{F}\| > \varepsilon$)**:**

  Compute: $\mathrm{Jacobian}\,[J] = \begin{bmatrix} \frac{\partial F^1}{\partial \kappa_d^1} & \cdot & \cdot & \cdot & \frac{\partial F^1}{\partial \kappa_d^q} \\ \cdot & \cdot & & & \cdot \\ \cdot & & \cdot & & \cdot \\ \cdot & & & \cdot & \cdot \\ \frac{\partial F^q}{\partial \kappa_d^1} & \cdot & \cdot & \cdot & \frac{\partial F^q}{\partial \kappa_d^q} \end{bmatrix}$

  Solve: $[J] \cdot \begin{Bmatrix} \delta\kappa_d^1 \\ \cdot \\ \cdot \\ \cdot \\ \delta\kappa_d^q \end{Bmatrix} = \begin{Bmatrix} F^1 \\ \cdot \\ \cdot \\ \cdot \\ F^q \end{Bmatrix}$

  Do $\alpha = 1$ **to** q**:**

    Update: $\Delta\kappa_d^\alpha$, $\Delta\boldsymbol{\kappa}_d^\alpha$, $\boldsymbol{\kappa}_d^\alpha$, $\Delta\boldsymbol{\kappa}_r^\alpha$, $\boldsymbol{\kappa}_r^\alpha$

    Update: $\boldsymbol{\xi}^\alpha$, $\mathbf{X}^\alpha$, S_ξ^α

    Update: $F^\alpha = \|\boldsymbol{\xi}^\alpha - \mathbf{X}^\alpha\| - S_\xi^\alpha\, l_d \left(\frac{\Delta\kappa_d^\alpha}{\Delta t\,\dot{\gamma}_0^\alpha}\right)^m$

  End do

  $\mathbf{F} = \left[F^1, \ldots, F^q\right]^T$

End while

Appendix C. Expression of the Jacobian matrix in the Prager-type model

Giving inputs at an increment p, it is necessary to compute the Jacobian (see Alg. 1) in order to update the stresses at the increment $p+1$. For simplicity, equations are written for the described 2D problem. The Newton-Raphson (Besson et al., 2010) aims at solving the equation:

$$F^\alpha = \|\boldsymbol{\xi}^\alpha - \mathbf{X}^\alpha\| - S_\xi^\alpha \, l_d \left(\frac{\Delta\kappa_d^\alpha}{\Delta t \, \dot{\gamma}_0^\alpha}\right)^m = \xi_{eq}^\alpha - \xi_c^\alpha \tag{C.1}$$

at the iteration $k+1$ knowing a non-convergence at the iteration k. The implementation is done in order to have a continuum tangent modulus. In this sense, the following equations are used:

$$\delta F^\alpha = \delta\xi_{eq}^\alpha - \delta\xi_c^\alpha \tag{C.2}$$

with

$$\delta\xi_{eq}^\alpha = \frac{\partial \|\boldsymbol{\xi}^\alpha - \mathbf{X}^\alpha\|}{\partial \boldsymbol{\xi}^\alpha} \cdot \delta\boldsymbol{\xi}^\alpha + \frac{\partial \|\boldsymbol{\xi}^\alpha - \mathbf{X}^\alpha\|}{\partial \mathbf{X}^\alpha} \cdot \delta\mathbf{X}^\alpha = \frac{[\boldsymbol{\xi}^\alpha - \mathbf{X}^\alpha]_{p+1}^k}{[\|\boldsymbol{\xi}^\alpha - \mathbf{X}^\alpha\|]_{p+1}^k} \cdot (\delta\boldsymbol{\xi}^\alpha - \delta\mathbf{X}^\alpha) \tag{C.3}$$

Based on:

$$\delta\boldsymbol{\kappa}_d^\alpha = \frac{\delta\kappa_d^\alpha}{l_d} \frac{[\boldsymbol{\xi}^\alpha - \mathbf{X}^\alpha]_{p+1}^k}{[\|\boldsymbol{\xi}^\alpha - \mathbf{X}^\alpha\|]_{p+1}^k} \tag{C.4}$$

it is deduced that:

$$\delta\mathbf{X}^\alpha = H_p l_d^2 \, \delta\boldsymbol{\kappa}_d^\alpha = H_p l_d^2 \frac{\delta\kappa_d^\alpha}{l_d} \frac{[\boldsymbol{\xi}^\alpha - \mathbf{X}^\alpha]_{p+1}^k}{[\|\boldsymbol{\xi}^\alpha - \mathbf{X}^\alpha\|]_{p+1}^k} \tag{C.5}$$

$$\dot{\boldsymbol{\xi}}^\alpha = \mathbf{A}^{\alpha\alpha} \cdot (\dot{\boldsymbol{\kappa}}^\alpha - \dot{\boldsymbol{\kappa}}_d^\alpha) \Rightarrow \delta\boldsymbol{\xi}^\alpha = \delta\mathbf{A}^{\alpha\alpha} \cdot \left(\Delta\boldsymbol{\kappa}^\alpha - [\Delta\boldsymbol{\kappa}_d^\alpha]_{p+1}^k\right) + [\mathbf{A}^{\alpha\alpha}]_{p+1}^k \cdot (\delta\boldsymbol{\kappa}^\alpha - \delta\boldsymbol{\kappa}_d^\alpha) \tag{C.6}$$

$\Delta\boldsymbol{\kappa}^\alpha$ is constant during the iterations at the increment $p+1$ so that $\delta\boldsymbol{\kappa}^\alpha = \mathbf{0}$. For this reason:

$$\delta\mathbf{A}^{\alpha\alpha} = \frac{\partial \mathbf{A}^{\alpha\alpha}}{\partial \boldsymbol{\kappa}_d^\alpha} \cdot \delta\boldsymbol{\kappa}_d^\alpha \tag{C.7}$$

$$\begin{aligned} \frac{\partial \mathbf{A}^{\alpha\alpha}}{\partial \boldsymbol{\kappa}_d^\alpha} &= (n-1)(n-2) X_0 \, l_{en}^n \, |\mathbf{s}^\alpha \cdot (\boldsymbol{\kappa}^\alpha - \boldsymbol{\kappa}_d^\alpha)|^{n-3} \frac{\partial \, |\mathbf{s}^\alpha \cdot (\boldsymbol{\kappa}^\alpha - \boldsymbol{\kappa}_d^\alpha)|}{\partial \boldsymbol{\kappa}_d^\alpha} \otimes \mathbf{s}^\alpha \otimes \mathbf{s}^\alpha \\ &= -(n-1)(n-2) X_0 \, l_{en}^n \, |\mathbf{s}^\alpha \cdot (\boldsymbol{\kappa}^\alpha - \boldsymbol{\kappa}_d^\alpha)|^{n-4} \, \mathbf{s}^\alpha \cdot (\boldsymbol{\kappa}^\alpha - \boldsymbol{\kappa}_d^\alpha) \, \mathbf{s}^\alpha \otimes \mathbf{s}^\alpha \otimes \mathbf{s}^\alpha \end{aligned} \tag{C.8}$$

$$\delta\mathbf{A}^{\alpha\alpha} = -(n-1)(n-2) X_0 \, l_{en}^n \, |\mathbf{s}^\alpha \cdot (\boldsymbol{\kappa}^\alpha - \boldsymbol{\kappa}_d^\alpha)|^{n-4} \, [\mathbf{s}^\alpha \cdot (\boldsymbol{\kappa}^\alpha - \boldsymbol{\kappa}_d^\alpha)] \, [\mathbf{s}^\alpha \cdot \delta\boldsymbol{\kappa}_d^\alpha] \, \mathbf{s}^\alpha \otimes \mathbf{s}^\alpha \tag{C.9}$$

It leads to:

$$\begin{cases} \delta\boldsymbol{\xi}^\alpha & = -(n-1)(n-2) X_0 \, l_{en}^n \, |\mathbf{s}^\alpha \cdot (\boldsymbol{\kappa}^\alpha - \boldsymbol{\kappa}_d^\alpha)|^{n-4} \, [\mathbf{s}^\alpha \cdot (\boldsymbol{\kappa}^\alpha - \boldsymbol{\kappa}_d^\alpha)] \, [\mathbf{s}^\alpha \cdot \delta\boldsymbol{\kappa}_d^\alpha] \, (\mathbf{s}^\alpha \otimes \mathbf{s}^\alpha) \cdot \left(\Delta\boldsymbol{\kappa}^\alpha - [\Delta\boldsymbol{\kappa}_d^\alpha]_{p+1}^k\right) \\ & \quad - (n-1) \, X_0 \, l_{en}^n \left[|\mathbf{s}^\alpha \cdot (\boldsymbol{\kappa}^\alpha - \boldsymbol{\kappa}_d^\alpha)|^{n-2} \, \mathbf{s}^\alpha \otimes \mathbf{s}^\alpha\right] \cdot \delta\boldsymbol{\kappa}_d^\alpha \\ & = -(n-1) X_0 \, l_{en}^n \, |\mathbf{s}^\alpha \cdot (\boldsymbol{\kappa}^\alpha - \boldsymbol{\kappa}_d^\alpha)|^{n-4} \, [\mathbf{B}_L^{\alpha\alpha}]_{p+1}^k \cdot \delta\boldsymbol{\kappa}_d^\alpha = -\, [\mathbf{A}_L^{\alpha\alpha}]_{p+1}^k \cdot \delta\boldsymbol{\kappa}_d^\alpha \end{cases}$$

(C.10)

with

$$[\mathbf{B}_L^{\alpha\alpha}]_{p+1}^k = (n-2)\left[\mathbf{s}^\alpha \cdot (\boldsymbol{\kappa}^\alpha - \boldsymbol{\kappa}_d^\alpha)\right]\left[\mathbf{s}^\alpha \cdot \left(\Delta\boldsymbol{\kappa}^\alpha - [\Delta\boldsymbol{\kappa}_d^\alpha]_{p+1}^k\right)\right]\mathbf{s}^\alpha \otimes \mathbf{s}^\alpha + \left|\mathbf{s}^\alpha \cdot (\boldsymbol{\kappa}^\alpha - \boldsymbol{\kappa}_d^\alpha)\right|^2 \mathbf{s}^\alpha \otimes \mathbf{s}^\alpha \quad \text{(C.11)}$$

Eq. (C.3) becomes:

$$\delta\xi_{eq}^\alpha = -\frac{[\boldsymbol{\xi}^\alpha - \mathbf{X}^\alpha]_{p+1}^k}{[\|\boldsymbol{\xi}^\alpha - \mathbf{X}^\alpha\|]_{p+1}^k} \cdot \left([\mathbf{A}_L^{\alpha\alpha}]_{p+1}^k + H_p l_d^2 \mathbf{I}\right) \cdot \frac{\delta\kappa_d^\alpha}{l_d} \frac{[\boldsymbol{\xi}^\alpha - \mathbf{X}^\alpha]_{p+1}^k}{[\|\boldsymbol{\xi}^\alpha - \mathbf{X}^\alpha\|]_{p+1}^k} \quad \text{(C.12)}$$

where $\mathbf{I}$ is the second order identity tensor.

$$\begin{aligned}
\delta\xi_c^\alpha &= \delta\left\{S_\xi^\alpha\, l_d \left(\frac{\Delta\kappa_d^\alpha}{\Delta t\,\dot\gamma_0^\alpha}\right)^m\right\} = \delta\left\{S_\xi^\alpha\, l_d\, R^\alpha\right\} \\
&= l_d\left[\delta S_\xi^\alpha\right][R^\alpha]_{p+1}^k + l_d\left[S_\xi^\alpha\right]_{p+1}^k[\delta R^\alpha] \\
&= l_d\left[\sum_{\beta=1}^q H_\xi\,\delta\kappa_d^\beta\right][R^\alpha]_{p+1}^k + l_d\left[S_\xi^\alpha\right]_{p+1}^k \frac{m}{\Delta t\,\dot\gamma_0^\alpha}\left(\frac{\Delta\kappa_d^\alpha}{\Delta t\,\dot\gamma_0^\alpha}\right)^{m-1}\delta\kappa_d^\alpha \\
&= l_d\left[\sum_{\beta=1}^q H_\xi\,\delta\kappa_d^\beta\right][R^\alpha]_{p+1}^k + l_d\left[S_\xi^\alpha\right]_{p+1}^k \frac{C_R^\alpha}{\Delta t}\,\delta\kappa_d^\alpha
\end{aligned} \quad \text{(C.13)}$$

It follows that:

$$\delta F^\alpha = \sum_{\beta=1}^q \left[-\frac{[\boldsymbol{\xi}^\alpha - \mathbf{X}^\alpha]_{p+1}^k}{[\|\boldsymbol{\xi}^\alpha - \mathbf{X}^\alpha\|]_{p+1}^k} \cdot \left\{[\mathbf{A}_L^{\alpha\alpha}]_{p+1}^k + H_p l_d^2\mathbf{I}\right\} \cdot \frac{[\boldsymbol{\xi}^\alpha - \mathbf{X}^\alpha]_{p+1}^k}{[\|\boldsymbol{\xi}^\alpha - \mathbf{X}^\alpha\|]_{p+1}^k}\right]\frac{\delta^{\alpha\beta}}{l_d}\delta\kappa_d^\beta - \sum_{\beta=1}^q\left[H_\xi\, l_d\,[R^\alpha]_{p+1}^k + l_d\left[S_\xi^\alpha\right]_{p+1}^k\frac{C_R^\alpha}{\Delta t}\delta^{\alpha\beta}\right]\delta\kappa_d^\beta \quad \text{(C.14)}$$

The terms of the Jacobian are then written as:

$$\left[J^{\alpha\beta}\right] = \left[-\frac{[\boldsymbol{\xi}^\alpha - \mathbf{X}^\alpha]_{p+1}^k}{[\|\boldsymbol{\xi}^\alpha - \mathbf{X}^\alpha\|]_{p+1}^k} \cdot \left\{[\mathbf{A}_L^{\alpha\alpha}]_{p+1}^k + H_p l_d^2\mathbf{I}\right\} \cdot \frac{[\boldsymbol{\xi}^\alpha - \mathbf{X}^\alpha]_{p+1}^k}{[\|\boldsymbol{\xi}^\alpha - \mathbf{X}^\alpha\|]_{p+1}^k}\right]\frac{\delta^{\alpha\beta}}{l_d} - \left[H_\xi\, l_d\,[R^\alpha]_{p+1}^k + l_d\left[S_\xi^\alpha\right]_{p+1}^k\frac{C_R^\alpha}{\Delta t}\delta^{\alpha\beta}\right] \quad \text{(C.15)}$$

Finally, equation:

$$[F^\alpha]_{p+1}^{k+1} = [F^\alpha]_{p+1}^k + \delta F^\alpha = 0 \quad \text{(C.16)}$$

leads to:

$$\{\delta\kappa_d\} = -\,[J]^{-1}\left\{[F]_{p+1}^k\right\} \quad \text{(C.17)}$$

References

Abatour, M. and Forest, S. (2023). Strain gradient plasticity based on saturating variables. *Eur. J. Mech. A/Solids*, page 105016.

Acharya, A. and Bassani, J. L. (2000). Lattice incompatibility and a gradient theory of crystal plasticity. *J. Mech. Phys. Solids*, 48(8):1565–1595.

Aifantis, E. C. (1984). On the microstructural origin of certain inelastic models. *J. Eng. Mater. Technol.*, 106(4):326.

Aifantis, E. C. (1987). The physics of plastic deformation. *Int. J. Plast.*, 3(3):211–247.

Amouzou-Adoun, Y. A., Jebahi, M., Fivel, M., Forest, S., Lecomte, J. S., Schuman, C., and Abed-Meraim, F. (2023). On elastic gaps in strain gradient plasticity: 3D discrete dislocation dynamics investigation. *Acta Mater.*, 252:118920.

Arsenlis, A. and Parks, D. M. (1999). Crystallographic aspects of geometrically-necessary and statistically-stored dislocation density. *Acta Mater.*, 47(5):1597–1611.

Asaro, R. J. (1975). Elastic-plastic memory and kinematic-type hardening. *Acta Metall.*, 23(10):1255–1265.

Ashby, M. F. (1970). The deformation of plastically non-homogeneous materials. *Philos. Mag.*, 21(170):399–424.

Bardella, L. (2010). Size effects in phenomenological strain gradient plasticity constitutively involving the plastic spin. *Int. J. Eng. Sci.*, 48(5):550–568.

Bardella, L. and Panteghini, A. (2015). Modelling the torsion of thin metal wires by distortion gradient plasticity. *J. Mech. Phys. Solids*, 78:467–492.

Bardella, L., Segurado, J., Panteghini, A., and Llorca, J. (2013). Latent hardening size effect in small-scale plasticity. *Model. Simul. Mater. Sci. Eng.*, 21(5).

Bayerschen, E. and Böhlke, T. (2016). Power-law defect energy in a single-crystal gradient plasticity framework: a computational study. *Comput. Mech.*, 58(1):13–27.

Bayerschen, E., Stricker, M., Wulfinghoff, S., Weygand, D., and Böhlke, T. (2015). Equivalent plastic strain gradient plasticity with grain boundary hardening and comparison to discrete dislocation dynamics. *Proc. R. Soc. A Math. Phys. Eng. Sci.*, 471(2184):20150388.

Besson, J., Cailletaud, G., Chaboche, J.-L., and Forest, S. (2010). *Non-Linear Mechanics of Materials*, volume 167 of *Solid Mechanics and Its Applications*. Springer Netherlands.

Bittencourt, E. (2018). On the effects of hardening models and lattice rotations in strain gradient crystal plasticity simulations. *Int. J. Plast.*, 108:169–185.

Bittencourt, E., Needleman, A., Gurtin, M. E., and Van der Giessen, E. (2003). A comparison of nonlocal continuum and discrete dislocation plasticity predictions. *J. Mech. Phys. Solids*, 51(2):281–310.

Busso, E. P., Meissonnier, F. T., and O'Dowd, N. P. (2000). Gradient-dependent deformation of two-phase single crystals. *J. Mech. Phys. Solids*, 48(11):2333–2361.

Byer, C. M. and Ramesh, K. T. (2013). Effects of the initial dislocation density on size effects in single-crystal magnesium. *Acta Mater.*, 61(10):3808–3818.

Cai, L., Jebahi, M., and Abed-Meraim, F. (2021). Strain localization modes within single crystals using finite deformation strain gradient crystal plasticity. *Crystals*, 11(10):1235.

Cai, W., Arsenlis, A., Weinberger, C. R., and Bulatov, V. V. (2006). A non-singular continuum theory of dislocations. *J. Mech. Phys. Solids*, 54:561–587.

Chaboche, J.-L. (1989). Constitutive equations for cyclic plasticity and cyclic viscoplasticity. *Int. J. Plast.*, 5(3):247–302.

Chang, H. J., Cordero, N. M., Déprés, C., Fivel, M., and Forest, S. (2016). Micromorphic crystal plasticity versus discrete dislocation dynamics analysis of multilayer pile-up hardening in a narrow channel. *Arch. Appl. Mech.*, 86(1-2):21–38.

Cordero, N. M., Forest, S., and Busso, E. P. (2013). Micromorphic modelling of grain size effects in metal polycrystals. *GAMM Mitteilungen*, 36(2):186–202.

Cordero, N. M., Gaubert, A., Forest, S., Busso, E. P., Gallerneau, F., and Kruch, S. (2010). Size effects in generalised continuum crystal plasticity for two-phase laminates. *J. Mech. Phys. Solids*, 58(11):1963–1994.

Cordero, Z. C., Knight, B. E., and Schuh, C. A. (2016). Six decades of the Hall-Petch effect - a survey of grain-size strengthening studies on pure metals. *Int. Mater. Rev.*, 61(8):495–512.

Croné, P., Gudmundson, P., and Faleskog, J. (2022). Strain gradient plasticity modelling of cyclic loading in dispersion hardened materials. *Eur. J. Mech. A/Solids*, 96:104741.

Cruzado, A., Ariza, M., Needleman, A., Ortiz, M., and Benzerga, A. (2024). A discrete dislocation analysis of size-dependent plasticity in torsion. *J. Mech. Phys. Solids*, page 105709.

Dahlberg, C. F. O. and Boåsen, M. (2019). Evolution of the length scale in strain gradient plasticity. *Int. J. Plast.*, 112:220–241.

Dahlberg, C. F. O. and Ortiz, M. (2019). Fractional strain-gradient plasticity. *Eur. J. Mech. A/Solids*, 75:348–354.

de Borst, R. (1993). A generalisation of J2-flow theory for polar continua. *Comput. Methods Appl. Mech. Eng.*, 103(3):347–362.

Dunstan, D. J. and Bushby, A. J. (2014). Grain size dependence of the strength of metals: The Hall-Petch effect does not scale as the inverse square root of grain size. *Int. J. Plast.*, 53:56–65.

E. O. Hall (1951). The deformation and ageing of mild steel: III discussion of results. *Proc. Phys. Soc. Sect. B*, 64:747–753.

El-Awady, J. A. (2015). Unravelling the physics of size-dependent dislocation-mediated plasticity. *Nat. Commun.*, 6:1–9.

El-Awady, J. A., Uchic, M. D., Shade, P. A., Kim, S. L., Rao, S. I., Dimiduk, D. M., and Woodward, C. (2013). Pre-straining effects on the power-law scaling of size-dependent strengthening in Ni single crystals. *Scr. Mater.*, 68:207–210.

El-Naaman, S. A., Nielsen, K. L., and Niordson, C. F. (2019). An investigation of back stress formulations under cyclic loading. *Mech. Mater.*, 130:76–87.

Fan, H., Wang, Q., El-Awady, J. A., Raabe, D., and Zaiser, M. (2021). Strain rate dependency of dislocation plasticity. *Nat. Commun.*, 12:1–12.

Fivel, M., Gosling, T. J., and Canova, G. R. (1996). Implementing image stresses in a 3D dislocation simulation. *Model. Simul. Mater. Sci. Eng.*, 4:581–596.

Fivel, M. C., Robertson, C. F., Canova, G. R., and Boulanger, L. (1998). Three-dimensional modeling of indent-induced plastic zone at a mesoscale. *Acta Mater.*, 46(17):6183–6194.

Fleck, N. A. and Hutchinson, J. W. (1997). Strain gradient plasticity. *Adv. Appl. Mech.*, 33:295–361.

Fleck, N. A. and Hutchinson, J. W. (2001). A reformulation of strain gradient plasticity. *J. Mech. Phys. Solids*, 49(10):2245–2271.

Fleck, N. A., Hutchinson, J. W., and Willis, J. R. (2014). Strain gradient plasticity under non-proportional loading. *Proc. R. Soc. A Math. Phys. Eng. Sci.*, 470(2170):0267.

Fleck, N. A., Hutchinson, J. W., and Willis, J. R. (2015). Guidelines for constructing strain gradient plasticity theories. *J. Appl. Mech. Trans. ASME*, 82(7):071002.

Fleck, N. A., Muller, G. M., Ashby, M. F., and Hutchinson, J. W. (1994). Strain gradient plasticity: Theory and experiment. *Acta Metall. Mater.*, 42(2):475–487.

Forest, S. (2008). Some links between Cosserat, strain gradient crystal plasticity and the statistical theory of dislocations. *Philos. Mag.*, 88(30-32):3549–3563.

Forest, S. (2009). Micromorphic Approach for Gradient Elasticity, Viscoplasticity, and Damage. *J. Eng. Mech.*, 135(3):117–131.

Forest, S. (2020). Continuum thermomechanics of nonlinear micromorphic, strain and stress gradient media. *Philos. Trans. R. Soc. A Math. Phys. Eng. Sci.*, 378(2170).

Forest, S. and Bertram, A. (2011). Formulations of Strain Gradient Plasticity. In *Mech. Gen. Contin.*, volume 53, pages 137–149.

Forest, S., Cailletaud, G., and Sievert, R. (1997). A Cosserat theory for elastoviscoplastic single crystals at finite deformation. *Arch. Mech.*, 49(4):705–736.

Forest, S. and Sievert, R. (2003). Elastoviscoplastic constitutive frameworks for generalized continua. *Acta Mech.*, 160(1-2):71–111.

Germain, P. (1973). The method of virtual power in continuum mechanics. Part 2: Microstructure. *SIAM J. Appl. Math.*, 25(3):556–575.

Gologanu, M., Leblond, J., and Devaux, J. (1997). *Recent extensions of Gurson's model for porous ductile metals*, volume 377, pages 61–130. Springer Vienna, CISM Courses and Lectures No. 377.

Gravell, J. D. and Ryu, I. (2020). Latent hardening/softening behavior in tension and torsion combined loadings of single crystal FCC micropillars. *Acta Mater.*, 190:58–69.

Gudmundson, P. (2004). A unified treatment of strain gradient plasticity. *J. Mech. Phys. Solids*, 52(6):1379–1406.

Gurtin, M. E. (2002). A gradient theory of single-crystal viscoplasticity that accounts for geometrically necessary dislocations. *J. Mech. Phys. Solids*, 50(1):5–32.

Gurtin, M. E. (2004). A gradient theory of small-deformation isotropic plasticity that accounts for the Burgers vector and for dissipation due to plastic spin. *J. Mech. Phys. Solids*, 52(11):2545–2568.

Gurtin, M. E. and Anand, L. (2009). Thermodynamics applied to gradient theories involving the accumulated plastic strain: The theories of Aifantis and Fleck and Hutchinson and their generalization. *J. Mech. Phys. Solids*, 57(3):405–421.

Gurtin, M. E., Anand, L., and Lele, S. P. (2007). Gradient single-crystal plasticity with free energy dependent on dislocation densities. *J. Mech. Phys. Solids*, 55(9):1853–1878.

Gurtin, M. E. and Reddy, B. D. (2009). Alternative formulations of isotropic hardening for Mises materials, and associated variational inequalities. *Contin. Mech. Thermodyn.*, 21(3):237–250.

Hidayetoglu, T. K., Pica, P. N., and Haworth, W. (1985). Aging dependence of the Bauschinger effect in aluminum alloy 2024. *Mater. Sci. Eng.*, 73:65–76.

Hua, F., Liu, D., Li, Y., He, Y., and Dunstan, D. (2021). On energetic and dissipative gradient effects within higher-order strain gradient plasticity: Size effect, passivation effect, and Bauschinger effect. *Int. J. Plast.*, 141:102994.

Hunter, A. and Koslowski, M. (2008). Direct calculations of material parameters for gradient plasticity. *J. Mech. Phys. Solids*, 56(11):3181–3190.

Hussein, A. M., Rao, S. I., Uchic, M. D., Dimiduk, D. M., and El-Awady, J. A. (2015). Microstructurally based cross-slip mechanisms and their effects on dislocation microstructure evolution in fcc crystals. *Acta Mater.*, 85:180–190.

Hutchinson, J. W. (2012). Generalizing J2 flow theory: Fundamental issues in strain gradient plasticity. *Acta Mech. Sin.*, 28(4):1078–1086.

Jebahi, M., Cai, L., and Abed-Meraim, F. (2020). Strain gradient crystal plasticity model based on generalized non-quadratic defect energy and uncoupled dissipation. *Int. J. Plast.*, 126:102617.

Jebahi, M. and Forest, S. (2021). Scalar-based strain gradient plasticity theory to model size-dependent kinematic hardening effects. *Contin. Mech. Thermodyn.*, 33(4):1223–1245.

Jebahi, M. and Forest, S. (2023). An alternative way to describe thermodynamically-consistent higher-order dissipation within strain gradient plasticity. *J. Mech. Phys. Solids*, 170:105103.

Jian, W. R., Xiao, M., Sun, W. C., and Cai, W. (2024). Prediction of yield surface of single crystal copper from discrete dislocation dynamics and geometric learning. *J. Mech. Phys. Solids*, 186:105577.

Jiang, M., Devincre, B., and Monnet, G. (2019). Effects of the grain size and shape on the flow stress: A dislocation dynamics study. *Int. J. Plast.*, 113:111–124.

Kiener, D., Motz, C., Grosinger, W., Weygand, D., and Pippan, R. (2010). Cyclic response of copper single crystal micro-beams. *Scr. Mater.*, 63:500–503.

Kooiman, M., Hütter, M., and Geers, M. (2015). Microscopically derived free energy of dislocations. *J. Mech. Phys. Solids*, 78:186–209.

Kuroda, M. and Needleman, A. (2023). Non-quadratic strain gradient plasticity theory and size effects in constrained shear. *J. Appl. Mech.*, 90:1–23.

Kuroda, M., Tvergaard, V., and Needleman, A. (2021). Constraint and size effects in confined layer plasticity. *J. Mech. Phys. Solids*, 149:104328.

Lee, S. H. and Schulz, K. (2023). A data-based derivation of the internal stress in the discrete-continuum transition regime of dislocation based plasticity. *Int. J. Plast.*, 170:103771.

Liu, D., He, Y., Dunstan, D. J., Zhang, B., Gan, Z., Hu, P., and Ding, H. (2013). Anomalous plasticity in the cyclic torsion of micron scale metallic wires. *Phys. Rev. Lett.*, 110:244301.

Martínez-Pañeda, E., Deshpande, V. S., Niordson, C. F., and Fleck, N. A. (2019). The role of plastic strain gradients in the crack growth resistance of metals. *J. Mech. Phys. Solids*, 126:136–150.

Mayeur, J. R. and McDowell, D. L. (2013). An evaluation of higher-order single crystal strength models for constrained thin films subjected to simple shear. *J. Mech. Phys. Solids*, 61(9):1935–1954.

Motz, C. and Dunstan, D. J. (2012). Observation of the critical thickness phenomenon in dislocation dynamics simulation of microbeam bending. *Acta Mater.*, 60:1603–1609.

Motz, C., Weygand, D., Senger, J., and Gumbsch, P. (2008). Micro-bending tests: A comparison between three-dimensional discrete dislocation dynamics simulations and experiments. *Acta Mater.*, 56:1942–1955.

Mu, Y., Zhang, X., Hutchinson, J. W., and Meng, W. J. (2016). Dependence of confined plastic flow of polycrystalline Cu thin films on microstructure. *MRS Commun.*, 6(3):289–294.

Mukherjee, A. and Banerjee, B. (2023). Strain gradient plasticity with nonlinear evolutionary energetic higher order stresses. *Int. J. Plast.*, 169:103739.

Niordson, C. F. and Hutchinson, J. W. (2003). On lower order strain gradient plasticity theories. *Eur. J. Mech. A/Solids*, 22(6):771–778.

Ohno, N. and Okumura, D. (2007). Higher-order stress and grain size effects due to self-energy of geometrically necessary dislocations. *J. Mech. Phys. Solids*, 55(9):1879–1898.

Panteghini, A. and Bardella, L. (2018). On the role of higher-order conditions in distortion gradient plasticity. *J. Mech. Phys. Solids*, 118:293–321.

Panteghini, A., Bardella, L., and Niordson, C. F. (2019). A potential for higher-order phenomenological strain gradient plasticity to predict reliable response under non-proportional loading. *Proc. R. Soc. A*, 475(2229):20190258.

Peach, M. and Koehler, J. S. (1950). The forces exerted on dislocations and the stress fields produced by them. *Phys. Rev.*, 80:436–439.

Petch, N. J. (1953). The cleavage strength of polycrystals. *J. Iron Steel Inst.*, 174:25–28.

Proudhon, H., Poole, W. J., Wang, X., and Bréchet, Y. (2008). The role of internal stresses on the plastic deformation of the Al-Mg-Si-Cu alloy AA6111. *Philos. Mag.*, 88(5):621–640.

Regueiro, R. A. (2010). On finite strain micromorphic elastoplasticity. *Int. J. Solids Struct.*, 47(6):786–800.

Reynolds, A. and Baxter, S. (2000). Kinematic hardening in a dispersion strengthened aluminum alloy: experiment and modeling. *Mater. Sci. Eng. A*, 285(1-2):265–279.

Robertson, C. F. and Fivel, M. C. (1999). Study of the submicron indent-induced plastic deformation. *J. Mater. Res.*, 14(6):2251–2258.

Ryu, I., Cai, W., Nix, W. D., and Gao, H. (2016). Anisotropic Size-Dependent Plasticity in Face-Centered Cubic Micropillars Under Torsion. *Jom*, 68(1):253–260.

Ryu, I., Gravell, J. D., Cai, W., Nix, W. D., and Gao, H. (2020). Intrinsic size dependent plasticity in BCC micro-pillars under uniaxial tension and pure torsion. *Extrem. Mech. Lett.*, 40:100901.

Scherer, J. M., Phalke, V., Besson, J., Forest, S., Hure, J., and Tanguy, B. (2020). Lagrange multiplier based vs micromorphic gradient-enhanced rate-(in)dependent crystal plasticity modelling and simulation. *Comput. Methods Appl. Mech. Eng.*, 372:113426.

Sharma, V., Rao, G., Sharma, S., and George, K. (2014). Low cycle fatigue behavior of AA2219-T87 at room temperature. *Mater. Perform. Charact.*, 3(1):103–126.

Shu, J. Y., Fleck, N. A., Van der Giessen, E., and Needleman, A. (2001). Boundary layers in constrained plastic flow: comparison of nonlocal and discrete dislocation plasticity. *J. Mech. Phys. Solids*, 49(6):1361–1395.

Simo, J. C. and Hughes, T. J. (1999). *Computational inelasticity*, volume 37. Springer.

Stallard, J. C., Vema, S., Grey, C. P., Deshpande, V. S., and Fleck, N. A. (2023). The strength of a constrained lithium layer. *Acta Mater.*, 260:119313.

Stölken, J. S. and Evans, A. G. (1998). A microbend test method for measuring the plasticity length scale. *Acta Mater.*, 46(14):5109–5115.

Stoltz, R. E. and Pelloux, R. M. (1976). The Bauschinger effect in precipitation strengthened aluminum alloys. *Metall. Trans. A*, 7(8):1295–1306.

Tagarielli, V. L. and Fleck, N. A. (2010). The Shear Response of a Thin Aluminum Layer. *J. Appl. Mech.*, 78(1):014505.

Taillard, R. and Pineau, A. (1982). Room temperature tensile properties of Fe-19wt.%Cr alloys precipitation hardened by the intermetallic compound NiAl. *Mater. Sci. Eng.*, 56(3):219–231.

Thompson, A. W. (1977). Effect of grain size on work hardening in nickel. *Acta Metall.*, 25(1):83–86.

Ugi, D., Zoller, K., Lukács, K., Fogarassy, Z., Groma, I., Kalácska, S., Schulz, K., and Ispánovity, P. D. (2024). Irreversible evolution of dislocation pile-ups during cyclic microcantilever bending. *Mater. Des.*, 238:112682.

Verdier, M., Fivel, M., and Groma, I. (1998). Mesoscopic scale simulation of dislocation dynamics in fcc metals: Principles and applications. *Model. Simul. Mater. Sci. Eng.*, 6:755–770.

Voyiadjis, G. Z. and Deliktas, B. (2009). Mechanics of strain gradient plasticity with particular reference to decomposition of the state variables into energetic and dissipative components. *Int. J. Eng. Sci.*, 47(11-12):1405–1423.

Voyiadjis, G. Z. and Song, Y. (2016). Effect of passivation on higher order gradient plasticity models for non-proportional loading : energetic and dissipative gradient components. *Philos. Mag.*, 6435:1–28.

Voyiadjis, G. Z. and Song, Y. (2019). Strain gradient continuum plasticity theories: Theoretical, numerical and experimental investigations. *Int. J. Plast.*, 121:21–75.

Wulfinghoff, S., Forest, S., and Böhlke, T. (2015). Strain gradient plasticity modeling of the cyclic behavior of laminate microstructures. *J. Mech. Phys. Solids*, 79:1–20.

Xiang, Y. and Vlassak, J. J. (2006). Bauschinger and size effects in thin-film plasticity. *Acta Mater.*, 54:5449–5460.

Xiao, Y., Chen, J., and Cao, J. (2012). A generalized thermodynamic approach for modeling nonlinear hardening behaviors. *Int. J. Plast.*, 38:102–122.

Xie, Y., Lei, J., Hu, J., Luo, T., Ma, C., and Liu, D. (2024). On the role of higher-order condition of strain gradient plasticity in the cyclic torsion of thin metallic wires : Experiments and modeling. *Mech. Mater.*, 193:105007.

Xie, Y., Lei, J., Hua, F., Hu, J., Liu, D., and He, Y. (2023). Size and passivation effects in the torsion of thin metallic wires. *Acta Mech. Sin.*, 39(2).

Xing, Z., Fan, H., Tang, J., Wang, B., and Kang, G. (2021). Molecular dynamics simulation on the cyclic deformation of magnesium single crystals. *Comput. Mater. Sci.*, 186:110003.

Yefimov, S., Van Der Giessen, E., and Groma, I. (2004). Bending of a single crystal: Discrete dislocation and nonlocal crystal plasticity simulations. *Model. Simul. Mater. Sci. Eng.*, 12:1069–1086.

Zecevic, M., Lebensohn, R. A., and Capolungo, L. (2023). Non-local large-strain FFT-based formulation and its application to interface-dominated plasticity of nano-metallic laminates. *J. Mech. Phys. Solids*, 173:105187.

Zhang, B., Nielsen, K. L., Hutchinson, J. W., and Meng, W. J. (2023). Toward the development of plasticity theories for application to small-scale metal structures. *Proc. Natl. Acad. Sci.*, 120(44):2017.

Zhou, C., Biner, S. B., and LeSar, R. (2010). Discrete dislocation dynamics simulations of plasticity at small scales. *Acta Mater.*, 58:1565–1577.

Zhu, D., Zhang, H., and Li, D. Y. (2011). Molecular dynamics simulation of Bauschinger's effect in deformed copper single crystal in different strain ranges. *J. Appl. Phys.*, 110(12).